A Comparative Study of the Ground State Transitions of CO and C i as Molecular Gas Tracers at High Redshift

Frias Castillo, Marta; Rybak, Matus; Hodge, Jacqueline A.; van der Werf, Paul; Smail, Ian; Butterworth, Joshua; Ikarashi, Soh; Jiménez-Andrade, E. F.; Liao, Cheng Lin; More Authors

DOI
10.3847/1538-4357/adc4e0

Publication date
2025

Document Version
Final published version

Published in
Astrophysical Journal

The Astrophysical Journal, 987:158 (16pp), 2025 July 10 https://doi.org/10.3847/1538-4357/adc4e0

A Comparative Study of the Ground State Transitions of CO and C I as Molecular Gas Tracers at High Redshift

Marta Frias Castillo[1], Matus Rybak[1,2,3], Jacqueline A. Hodge[1], Paul van der Werf[1], Ian Smail[4], Joshua Butterworth[1], Jasper Jansen[1], Theodoros Topkaras[5], Chian-Chou Chen[6], Scott C. Chapman[7], Axel Weiss[8], Hiddo Algera[9,10], Jack E. Birkin[11,12], Elisabete da Cunha[13,14], Jianhang Chen[15], Helmut Dannerbauer[16,17], Soh Ikarashi[18,19], E. F. Jiménez-Andrade[20], Cheng-Lin Liao[6,21], Eric J. Murphy[22], A. M. Swinbank[4], Fabian Walter[23,24], Gabriela Calistro Rivera[15], R. J. Ivison[14,25,26,27], and Claudia del P. Lagos[14,28,29]
[1] Leiden Observatory, Leiden University, P.O. Box 9513, 2300 RA Leiden, The Netherlands; friascastillom@strw.leidenuniv.nl
[2] Faculty of Electrical Engineering, Mathematics and Computer Science, Delft University of Technology, Mekelweg 4, 2628 CD Delft, The Netherlands
[3] SRON—Netherlands Institute for Space Research, Niels Bohrweg 4, 2333 CA Leiden, The Netherlands
[4] Centre for Extragalactic Astronomy, Department of Physics, Durham University, South Road, Durham DH1 3LE, UK
[5] I. Physikalisches Institut, Universität zu Köln, Zülpicher Str. 77, 50937 Köln, Germany
[6] Academia Sinica Institute of Astronomy and Astrophysics (ASIAA), No.1, Section 4, Roosevelt Road, Taipei 10617, Taiwan
[7] Department of Physics and Atmospheric Science, Dalhousie University, Halifax, Halifax, NS B3H 3J5, Canada
[8] Max Planck Institut für Radioastronomie, Auf dem Hügel 69, D-53121 Bonn, Germany
[9] Hiroshima Astrophysical Science Center, Hiroshima University, 1-3-1 Kagamiyama, Higashi-Hiroshima, Hiroshima 739-8526, Japan
[10] National Astronomical Observatory of Japan, 2-21-1, Osawa, Mitaka, Tokyo, Japan
[11] Department of Physics and Astronomy, Texas A&M University, 4242 TAMU, College Station, TX 77843-4242, USA
[12] George P. and Cynthia Woods Mitchell Institute for Fundamental Physics and Astronomy, Texas A&M University, 4242 TAMU, College Station, TX 77843-4242, USA
[13] International Centre for Radio Astronomy Research, University of Western Australia, 35 Stirling Hwy, Crawley, WA 6009, Australia
[14] ARC Centre of Excellence for All Sky Astrophysics in 3 Dimensions (ASTRO 3D), Australia
[15] European Southern Observatory (ESO), Karl-Schwarzschild-Straße 2, 85748 Garching bei München, Germany
[16] Instituto Astrofísica de Canarias (IAC), E-38205 La Laguna, Tenerife, Spain
[17] Dpto. Astrofísica, Universidad de la Laguna, E-38206 La Laguna, Tenerife, Spain
[18] Department of Physics, General Studies, College of Engineering, Nihon University, 1 Nakagawara, Tokusada, Tamuramachi, Koriyama, Fukushima, 963-8642, Japan
[19] National Astronomical Observatory of Japan, 2-21-1 Osawa, Mitaka, Tokyo, 181-8588, Japan
[20] Instituto de Radioastronomía y Astrofísica, Universidad Nacional Autónoma de México, Antigua Carretera a Pátzcuaro # 8701, Ex-Hda. San José de la Huerta, Morelia, Michoacán, México C.P. 58089, Mexico
[21] Graduate Institute of Astrophysics, National Taiwan University, Taipei 10617, Taiwan
[22] National Radio Astronomy Observatory, 520 Edgemont Road, Charlottesville, VA 22903, USA
[23] Max Planck Institute for Astronomy, Königstuhl 17, 69117, Heidelberg, Germany
[24] National Radio Astronomy Observatory, Pete V. Domenici Array Science Center, P.O. Box O, Socorro, NM 87801, USA
[25] European Southern Observatory (ESO), Karl-Schwarzschild-Straße 2, D-85748 Garching, Germany
[26] School of Cosmic Physics, Dublin Institute for Advanced Studies, 31 Fitzwilliam Place, Dublin D02 XF86, Ireland
[27] Institute for Astronomy, University of Edinburgh, Royal Observatory, Blackford Hill, Edinburgh EH9 3HJ, UK
[28] International Centre for Radio Astronomy Research (ICRAR), M468, University of Western Australia, 35 Stirling Hwy, Crawley, WA 6009, Australia
[29] Cosmic Dawn Center (DAWN), Rådmandsgade 62, DK-2200 København, Denmark
Received 2024 March 28; revised 2025 March 19; accepted 2025 March 23; published 2025 July 4

Abstract

The CO(1–0) and [C I](1–0) emission lines are well-established tracers of cold molecular gas mass in local galaxies. At high redshift, where the interstellar medium is likely to be denser, there have been limited direct comparisons of both ground-state transitions. We present a comparison of [C I](1–0) and CO(1–0) emission in 20 unlensed dusty, star-forming galaxies at $z \geqslant 2$–5. The CO(1–0)/[C I](1–0) ratio remains constant up to $z = 5$, supporting the reliability of [C I](1–0) as a gas–mass tracer. We use the CO(1–0), [C I](1–0), and 3 mm dust continuum measurements to cross–calibrate their respective gas mass conversion factors, finding no dependence of these factors on either redshift or infrared luminosity. Radiative transfer modeling shows that the warmer cosmic microwave background (CMB) at high redshift can significantly affect the [C I] as well as CO emission, which can change the derived molecular gas masses by up to 70% for the coldest kinetic gas temperatures expected. Nevertheless, the magnitude of the CMB effect on the CO/[C I] ratio is within the known scatter of the $L'_{\rm CO} - L'_{\rm [CI]}$ relation. Precisely determining the CMB effect on individual line intensities would require well-sampled spectral line energy distributions to robustly model the gas excitation conditions. Finally, we note that adopting a variable CO gas–mass conversion factor for different galaxy populations implies [C I](1–0) and dust conversion factors that differ from canonically assumed values. However, the revised conversion factors are consistent with expectations for (super)solar metallicities likely to be found in high-redshift dusty galaxies.

Unified Astronomy Thesaurus concepts: High-redshift galaxies (734); Interstellar medium (847); Molecular gas (1073); Submillimeter astronomy (1647)

1. Introduction

The cold gas content of galaxies is expected to be one of the main drivers of the cosmic star formation rate (SFR) density of the Universe. Deep, blind surveys over modest volumes of the cosmic gas density reveal an evolutionary trend resembling that of the cosmic SFR density (e.g., R. Decarli et al. 2020; F. Walter et al. 2020), with both quantities peaking at $z = 1$–3. Moreover, the gas fractions of star-forming galaxies have been shown to increase at earlier times (from ∼5% at $z \sim 0$ to ∼50% at $z \sim 3$), supporting the fact that the increased availability of molecular gas reservoirs at $z = 1$–3 is likely to be the primary factor driving the higher SFRs seen in the early Universe (e.g., L. J. Tacconi et al. 2010, 2020; A. Saintonge et al. 2013; M. Béthermin et al. 2015; R. Decarli et al. 2020; M. Dessauges-Zavadsky et al. 2020; J. E. Birkin et al. 2021).

The main component of the molecular gas, molecular hydrogen (H_2), cannot be excited in its rotational/vibrational transitions in the low temperatures of the interstellar medium (ISM) of galaxies due to the large separation between its energy levels (∼500 K). Therefore, studies have traditionally relied on observations of carbon monoxide (^{12}CO, hereafter CO) emission lines, particularly the ground $J = 1$–0 transition, as an alternative tracer of the cold molecular gas reservoirs of galaxies (e.g., P. M. Solomon & P. A. Vanden Bout 2005; L. J. Hainline et al. 2006; D. T. Frayer et al. 2011; R. J. Ivison et al. 2011; A. I. Harris et al. 2012; A. P. Thomson et al. 2012; M. S. Bothwell et al. 2014; M. T. Huynh et al. 2017; A. Saintonge et al. 2017). However, this tracer requires the assumption of a CO-to-H_2 conversion factor, $\alpha_{\rm CO}$, which increases with decreasing metallicity (e.g., A. D. Bolatto et al. 2013) and has been suggested to vary between normal, star-forming galaxies and starbursts (D. Downes & P. M. Solomon 1998). Due to the lack of sufficient data to independently derive $\alpha_{\rm CO}$ in most galaxies, it is often assumed to be bimodal, with $\alpha_{\rm CO} \sim 3.6\ M_\odot\ (\mathrm{K\,km\,s^{-1}\,pc^2})^{-1}$ for galaxies on the main sequence and $\sim 1\ M_\odot\ (\mathrm{K\,km\,s^{-1}\,pc^2})^{-1}$ for ULIRG-like, starburst galaxies (see A. D. Bolatto et al. 2013, for a review).

Further, due to the technical challenges of detecting the faint CO(1–0) line emission at high redshift, studies of molecular gas at high redshift commonly rely on the brighter mid–$J_{\rm up}$ CO lines (e.g., M. S. Bothwell et al. 2013; L. J. Tacconi et al. 2013; L. A. Boogaard et al. 2020; R. Decarli et al. 2020; J. E. Birkin et al. 2021). Obtaining molecular gas masses from these lines then depends on line excitation corrections that introduce additional uncertainty (e.g., M. S. Bothwell et al. 2013; C. L. Carilli & F. Walter 2013; C. E. Sharon et al. 2016; L. A. Boogaard et al. 2020; D. A. Riechers et al. 2020a; J. E. Birkin et al. 2021; M. Frias Castillo et al. 2023). At high redshift ($z > 3$), this is further complicated by the cosmic microwave background (CMB), which acts as an additional excitation source for the gas and reduces the contrast between the background and the CO line emission. This can bias the information derived from line intensity measurements and imaging of the CO gas distribution of high-redshift galaxies (E. da Cunha et al. 2013; Z.-Y. Zhang et al. 2016).

A separate way to indirectly estimate molecular gas masses is via the long wavelength dust-continuum emission (e.g., R. H. Hildebrand 1983; N. Scoville et al. 2016; M. Kaasinen et al. 2019; D. Liu et al. 2019; T.-M. Wang et al. 2022). Observations of the dust continuum are generally less observationally expensive, allowing for larger samples to be studied. This method, however, requires the assumption of a mass-weighted cold dust temperature—this is typically assumed to be $T_{\rm dust} = 25$ K, which is claimed to be a representative value for both local star-forming galaxies and high-redshift galaxies (N. Scoville et al. 2016, 2017). Further, it is also dependent on the gas-to-dust abundance ratio, which varies according to a number of factors, e.g., optical depth, geometry, galaxy metallicity, and dust grain properties (e.g., A. D. Bolatto et al. 2013; G. Popping & C. Péroux 2022; G. Popping et al. 2023).

The ground-state atomic carbon [C I](^{3}P$_1$-^{3}P$_0$) emission line ($\nu_{\rm rest} = 492.161$ GHz, hereafter [C I](1–0)) may provide a promising alternative direct molecular gas tracer (e.g., P. P. Papadopoulos et al. 2004; F. Walter et al. 2011). Early, simple plane-parallel modeling of star-forming regions predicted that the [C I] emission arose only from narrow gas layers between the CO and [C II] emitting regions (A. G. G. M. Tielens & D. Hollenbach 1985). However, subsequent observational work on nearby galaxies (e.g., J. Keene et al. 1997; R. Ojha et al. 2001; Q. Jiao et al. 2019) and theoretical work (M. Tomassetti et al. 2014) have shown CO and [C I] emission to be fully concomitant, with tightly correlated intensities over a wide range of environments. [C I] emission is typically found to be optically thin (M. Ikeda et al. 2002; A. Weiß et al. 2003; K. C. Harrington et al. 2021), which means it can probe high column density environments, while its energy above ground is sufficiently low (24 K) to trace the bulk of the cold gas content, proving itself as a powerful alternative tool to measuring total molecular gas masses. Furthermore, when combined with CO line ratios, the [C I] lines reflect ISM properties such as density and UV radiation field strength (e.g., D. J. Hollenbach & A. G. G. M. Tielens 1999; M. J. Kaufman et al. 2006; S. Alaghband-Zadeh et al. 2013; F. P. Israel et al. 2015; M. S. Bothwell et al. 2017; P. Andreani et al. 2018; F. Valentino et al. 2018, 2020).

As with CO(1–0), the warmer CMB can have a significant impact at high redshift, but so far this effect has not been studied observationally. At high redshift, the [C I] emission line luminosity is correlated with that of CO in a variety of galaxy populations, from star-forming galaxies on the main sequence (MS, G. Popping et al. 2017; F. Valentino et al. 2018, 2020; N. Bourne et al. 2019; L. Dunne et al. 2022) to more extreme submillimeter galaxies (SMGs; I. Smail et al. 1997; D. H. Hughes et al. 1998; J. A. Hodge & E. da Cunha 2020; S. Berta et al. 2023) and quasar (QSO) hosts at $z \sim 2.5$ up to $z \sim 4$ (F. Walter et al. 2011; S. Alaghband-Zadeh et al. 2013; M. S. Bothwell et al. 2017; C. Yang et al. 2017; P. Andreani et al. 2018; J. E. Birkin et al. 2021; G. Gururajan et al. 2023). Many of these studies, however, suffer from one or more of three shortcomings. First, several use galaxy-scale strong gravitationally lensed systems. This introduces potential differential magnification effects and biases studies toward the most extreme sources (e.g., C. Yang et al. 2017). Second, in many nonlensed galaxies, CO(1–0) is too faint to detect in reasonable exposure times. As a result, the majority of studies rely on $J_{\rm up} > 2$ CO line observations and need to assume uncertain excitation corrections, which result in uncertainties in the derived CO(1–0) luminosity of up to 0.5 dex (M. Frias Castillo et al. 2023). Finally, the few studies that have both [C I](1–0) and CO(1–0) ground-state transitions have relied on individual, targeted sources (e.g., A. L. R. Danielson et al. 2011), and it is thus challenging to draw statistically significant

conclusions. Recently, L. Dunne et al. (2022) compiled all of the available literature studies using CO(1–0), [C I](1–0) and dust to provide a cross-calibration for metal-rich galaxies from $z\sim0$ to $z\sim5$, arguing that a single [C I]-to-H_2 conversion factor is applicable for both main-sequence and starburst galaxies. However, the number of unlensed $z>2$ sources with both ground-state CO and [C I] observations in their compilation was still <10, suggesting the need for further investigation.

In this paper, we present Atacama Large Millimeter/submillimeter Array (ALMA) Band 3 and 4 observations of the [C I](1–0) emission line in a sample of 12 unlensed SMGs, which are part of a new VLA survey of molecular gas in massive star-forming galaxies at high redshift (M. Frias Castillo et al. 2023). SMGs are dusty, high-infrared-luminosity ($L_{\rm IR}>10^{12}$ $L_\odot$; B. Magnelli et al. 2012) galaxies harboring some of the most intense starbursts that have ever occurred (SFR ∼100–1000 $M_\odot\,{\rm yr}^{-1}$; B. Magnelli et al. 2012; A. M. Swinbank et al. 2014; E. da Cunha et al. 2015; U. Dudzevičiūtė et al. 2020; C.-L. Liao et al. 2024), fueled by large molecular gas reservoirs of 10^{10}–10^{11} $M_\odot$ (T. R. Greve et al. 2005; L. J. Tacconi et al. 2008; M. S. Bothwell et al. 2013; M. Aravena et al. 2016; J. E. Birkin et al. 2021; M. Frias Castillo et al. 2023). Such luminous, massive galaxies are therefore the ideal targets to detect the faint CO(1–0) line with current facilities without the need for gravitational lensing. Combined with eight previously published [C I](1–0) detections from galaxies in the parent sample (J. E. Birkin et al. 2021; C.-L. Liao et al. 2024, A. Huber 2025, in preparation), this makes a total of 20 high-redshift, unlensed SMGs with observation of the ground transition of both CO and [C I].

This paper is structured as follows: we present the sample and ALMA observations, line emission, and continuum detections in Section 2. In Section 3 we probe the relation between the [C I] and infrared luminosities, as well as the relation between the CO(1–0) and [C I](1–0) luminosities. We use line and line-to-continuum ratios to constrain the physical conditions in the ISM of our galaxies, and present a cross-calibration of [C I] as a gas mass tracer through a comparison with CO(1–0) and dust-continuum emission. We then model the effect of the CMB on line emission at high redshift. Finally, we present a discussion of our results in Section 4 and our conclusions in Section 5. Throughout this paper we assume a standard ΛCDM cosmology with $H_0=67.8\,{\rm km\,s^{-1}\,Mpc^{-1}}$, $\Omega_{\rm M}=0.310$, and $\Omega_\Lambda=0.690$ (Planck Collaboration et al. 2016).

2. Data Reduction and Results

2.1. Sample

We analyze [C I](1–0) observations of 20 galaxies selected from an ongoing Karl G. Jansky Very Large Array (JVLA) survey, in which a total of 30 sources have been observed in CO(1–0) line emission in the *K* and *Ka* bands (M. Frias Castillo et al. 2023). The targets were selected from a sample of sources detected within $4\,{\rm deg}^2$ of SCUBA-2 850 μm imaging in the UKIDSS Ultra Deep Survey (UDS), Cosmological Evolution Survey (COSMOS), Chandra Deep Field North (CDFN), and Extended Groth Strip (EGS) fields from the S2CLS (J. E. Geach et al. 2017) and S2COSMOS (J. M. Simpson et al. 2019) surveys. The brightest submillimeter sources in these fields were subsequently followed up with ALMA (AS2UDS, S. M. Stach et al. 2018; AS2COSMOS; J. M. Simpson et al. 2020) and the Submillimeter Array (SMA) (EGS, CDFN, R. Hill et al. 2018) continuum imaging and further targeted with blind line scans using ALMA or NOEMA to obtain precise redshifts (J. E. Birkin et al. 2021; C.-C. Chen et al. 2022; C.-L. Liao et al. 2024, A. Huber 2025, in preparation). We refer the reader to M. Frias Castillo et al. (2023) for further details of the sample selection. Of the original parent sample, eight sources have published [C I](1–0) emission line detections (J. E. Birkin et al. 2021; C.-L. Liao et al. 2024), and we present new ALMA Band 3 and 4 observations for 12 more sources. Our sample thus comprises a total of 20 sources with [C I](1–0) and CO(1–0) line observations. Our sources are not strongly gravitationally lensed. C.-C. Chen et al. (2022) modeled the foreground gravitational fields of a subsample of the sample presented in this paper, finding that at most 10% could be gravitationally lensed with $\mu\geqslant2$. Further, the available subarcsecond ALMA imaging (e.g., S. M. Stach et al. (2019) for the UDS field, beam FWHM 0.″3) reveals compact morphologies (i.e., no multiple images, and no Einstein arcs). A significant fraction of our sources have Hubble Space Telescope imaging, and some have JWST imaging (e.g., AS2COS0001.1, AS2COS0002.1, and AS2COS0066.1) - none of these high-resolution images reveal lensing morphology. Only one source (AS2COS0001.1) shows potential evidence for a massive foreground galaxy that could imply it is lensed, but the extant optical/near-IR (including Spitzer and UKIRT) imaging does not show other foreground galaxies for the rest of the sample. The requirement that the sources be unlensed implies that the targets have large infrared luminosities, $L_{\rm IR}\sim10^{13}L_\odot$ (see Section 3).

2.2. JVLA CO(1–0) Data

Observations of the CO(1–0) emission (rest-frame frequency: $\nu_{\rm rest}=115.2712$ GHz) in our sample were carried out with the JVLA between 2021 March and 2024 January (project 21A-254, P.I.: Hodge). The *K*- or *Ka*-band receivers were used in combination with the WIDAR correlator configured to 8 bit sampling mode to observe a contiguous bandwidth of 2 GHz (dual polarization) at 2 MHz spectral resolution. Eight of the SMGs in this sample have CO(1–0) fluxes or upper limits reported in M. Frias Castillo et al. (2023), so we take the line luminosities and recalculate the upper limits for consistency with our analysis (see Section 2.4 for details on the flux extraction). For the rest of the sample, we calibrated the new data and obtained fluxes following M. Frias Castillo et al. (2023). The final line luminosities are reported in Table 2.

2.3. ALMA Data and Reduction

We obtained ALMA Band 3 and 4 observations during Cycle 8 (Project ID: 2021.1.01342.S). Data were collected in configurations C43–1/C43–2 between 2022 March 1 and 22.

We adopt calibrations performed in the second level of quality assurance (QA2). Flagging and calibrations were done using CASA version 6.2.1.7 (pipeline version: 2021.2.0.128, J. P. McMullin et al. 2007), which was also used for imaging. We first subtracted the continuum using the task UVCONTSUB in CASA after excluding the channels containing line emission. A priori, we used the line widths of the mid–$J_{\rm up}$ CO line emission reported in J. E. Birkin et al. (2021) and C.-L. Liao et al. (2024) and masked channels within ±2× the full width at half-maximum (FWHM) of the expected line, centered on the expected frequency of the [C I](1–0) line. We then imaged the

line-free channels in the continuum-subtracted image cubes to verify that all emission had been fully removed. No further continuum subtraction was necessary.

The continuum-subtracted visibilities were then imaged and cleaned using the TCLEAN algorithm in CASA, with a cleaning threshold of 2σ. We adopted natural weighting to maximize the signal-to-noise ratio (SNR) of the detections, which resulted in final beam sizes ranging from $2\farcs6$ to $4\farcs7$ (Table 1) at FWHM. At this resolution, the targeted galaxies are not (or only marginally) spatially resolved. We binned the data cubes spectrally to channels of 60 km s^{-1} to increase the SNR. The resulting data cubes reach a noise level of 0.2–0.5 mJy beam^{-1} per channel (see Table 1), estimated over the emission-free region of the channels.

2.4. [C I](1–0) Line and Continuum Detections

We began by collapsing the cleaned line cubes over the velocity width of the corresponding mid–$J_{\rm up}$ CO line from J. E. Birkin et al. (2021) or C.-L. Liao et al. (2024). This allows us to initially assess whether there is a spatial offset between the [C I] emission and the coordinates given in Table 1, derived from the ALMA and SMA continuum imaging (S. M. Stach et al. 2018; J. M. Simpson et al. 2020, A. Huber 2025, in preparation). Only AS2COS0001.1 and AS2COS0002.1 show an offset of $\sim 0\farcs5$. This offset might be caused by the low SNR of the emission in AS2COS0002.1. In the case of AS2COS0001.1, the source has a known companion only a few arcseconds away (C.-C. Chen et al. 2022), which we do not resolve due to the resolution of our observations and might skew the position of the peak emission. We extract the line spectra from the position of the peak emission using an aperture of $5''$ in diameter to maximize the SNR. We detect [C I](1–0) emission in 10 out of the 12 sources in the new [C I](1–0) sample. The line emission from AS2COS0002.1, AS2COS0014.1, and AS2COS0066.1 is just above the 2σ threshold, and they are only a marginal detection. The undetected sources, AS2COS0009.1 and AS2COS0044.1, are among the faintest far-infrared sources in the sample, which may explain their non-detections (Table 2). For the detected sources, the FWHM was derived from a single-Gaussian fitting to the spectra shown in Figure 1.

To avoid any bias due to line structure and to be consistent with the analysis performed for CO(1–0) in M. Frias Castillo et al. (2023), we derive line fluxes using the intensity-weighted (zeroth-moment) maps collapsed over a velocity range twice the corresponding mid–$J_{\rm up}$ CO line width for each source (J. E. Birkin et al. 2021; C.-L. Liao et al. 2024):

$$M_0 = I_{\rm CO} = \int I_\nu d\nu. \quad (1)$$

The median line width ratio of CO(4–3) or CO(3–2) to [C I](1–0) is 1.0 ± 0.1, and therefore the choice of FWHM (CO or [C I]) does not systematically impact the final recovered flux. Additionally, for the sources for which the SNR of the CO(1–0) data allows the fitting of a Gaussian profile to derive the FWHM, both the [C I](1–0) and CO(1–0) emission lines show consistent FWHM ($\rm FWHM_{[C\,I](1-0)}/FWHM_{CO(1-0)} = 1.03 \pm 0.3$).

In order to determine the optimal aperture to obtain the line fluxes, we perform a curve-of-growth analysis on these zeroth-moment maps by extracting flux densities from a set of circular apertures of increasing diameter, from $1\farcs5$ to $40''$. We find that an aperture of diameter $2\times$ the synthesized beam FWHM recovers most of the line flux while maximizing the SNR, so we adopt that aperture size to extract final fluxes. This is consistent with the fluxes obtained using the CASA task IMFIT, which conducts 2D Gaussian fitting on the zeroth-moment maps. For the two sources without detections, AS2COS0009.1 and AS2COS0044.1, we place 3σ upper limits on the emission by calculating the rms over an aperture covering a region of the zeroth-moment map away from the position of the target, and then correcting for an aperture of $2\times$ the synthesized beam size. We extract continuum fluxes in a similar manner by using a circular aperture of size $2\times$ the synthesized beam size on the continuum images. The final fluxes and FWHM are compiled in Table 2.[30]

We convert the [C I] line intensities into line luminosities following P. M. Solomon & P. A. Vanden Bout (2005):

$$L'_{\rm [CI](1-0)} = 3.25 \times 10^7\, I_{\rm [CI]}\, \nu^{-2}_{\rm obs}\, D^2_{\rm L}\, (1+z)^{-3} \times {\rm K\,km\,s^{-1}\,pc^2}, \quad (2)$$

where $I_{\rm [C\,I]}$ is the integrated line flux from the zeroth-moment map in Jy km s^{-1}, $\nu_{\rm obs}$ is the observed frequency in GHz and $D_{\rm L}$ is the luminosity distance in Mpc. We derive line luminosities in the range <0.47–3.1×10^{10} K km s^{-1} pc^2. Combined with the eight sources with published [C I](1–0) luminosities, our total sample spans the luminosity range <0.47–5.1×10^{10} K km s^{-1} pc^2 (see Table 2).

3. Analysis

3.1. [C I] Line Luminosities

First, we put the [C I] luminosities of the galaxies in our sample in the context of other low- and high-redshift observations. Figure 2 (left) shows the $L'_{\rm [CI](1-0)}$ line luminosities as a function of infrared luminosity, $L_{\rm IR}$. $L_{\rm IR}$ was estimated through spectral energy distribution (SED) fitting with MAGPHYS (A. J. Battisti et al. 2019), integrating over 8–1000 μm. For details of the photometry used, we refer the reader to J. M. Simpson et al. (2020) for sources in AS2COSMOS, U. Dudzevičiūtė et al. (2020) for AS2UDS, and M. Frias Castillo et al. (2023) for sources in the CDFN and EGS fields. If we take $L'_{\rm [CI](1-0)}$ and $L_{\rm IR}$ as proxies for gas mass and SFR, respectively, their relation is equivalent to the spatially integrated Schmidt–Kennicutt relation (M. Schmidt 1959; R. C. Kennicutt 1998; R. C. Kennicutt & N. J. Evans 2012). We compare them with the local ULIRGs from D. Liu et al. (2019), J. Kamenetzky et al. (2016) and I. Montoya Arroyave et al. (2023), the $z \sim 1$ MS galaxies from F. Valentino et al. (2018) and L. A. Boogaard et al. (2020), and the SMGs from F. Walter et al. (2011), A. L. R. Danielson et al. (2011), S. Alaghband-Zadeh et al. (2013); M. S. Bothwell et al. (2017), R. Cañameras et al. (2018), K. C. Harrington et al. (2018), N. P. H. Nesvadba et al. (2019), H. Dannerbauer et al. (2019)

[30] AS2COS0001.1 and AS2COS0008.1 have companion galaxies nearby (C.-C. Chen et al. 2022), which we cannot resolve at the resolution of our observations. Although the bulk of the emission is most likely dominated by the primary source, the [C I] line flux densities are likely overestimated. Since the CO(1–0) measured fluxes also suffer from the same problem, we do not correct the fluxes presented and treat both sources as a single target.

Table 1
Target Sample and Details of the New [C I](1–0) ALMA Observations

Target	R.A. (J2000)	Decl. (J2000)	z	Date	$\nu_{\rm obs}$ (GHz)	rms per Channel [a] (mJy beam^{-1})	Beam (maj × min, PA)	Phase Calibrator	Flux Calibrator
AS2COS0001.1	10:00:08.0	+02:26:12.3	4.625	05-03-2022	87.5	0.32	4.″6 × 3.″3, −66°	J0948+0022	J1058+0133
AS2COS0002.1	10:00:15.6	+02:15:49.0	4.595	05-03-2022	88.0	0.33	4.″7 × 3.″2, −66°	J0948+0022	J1058+0133
AS2COS0008.1	10:02:49.2	+02:32:55.5	3.581	02-03-2022	107.4	0.25	3.″5 × 3.″0, 85°	J1008-0029	J1058+0133
AS2COS0009.1	10:00:28.7	+02:32:03.6	2.260	02-03-2022	151.0	0.25	2.″42 × 2.″1, −73°	J0948+0022	J1058+0133
AS2COS0014.1	10:01:41.0	+02:04:04.9	2.921	21-03-2022	126.0	0.39	3.″7 × 2.″1, −60°	J0948+0022	J1058+0133
AS2COS0023.1	09:59:42.9	+02:29:38.2	4.341	05-03-2022	92.2	0.33	4.″4 × 3.″2, 75°	J0948+0022	J1058+0133
AS2COS0044.1	9:59:10.3	+02:48:55.7	2.580	07-03-2022	138.2	0.20	4.″3 × 3.″1, 75°	J1016+0513	J1058+0133
AS2COS0065.1	09:58:40.3	+02:05:14.7	2.414	07-03-2022	144.2	0.20	2.″8 × 2.″0, 68°	J0948+0022	J0854+2006
AS2COS0066.1	09:59:46.6	+01:57:15.1	3.247	05-03-2022	115.1	0.46	3.″1 × 2.″6, 80°	J0948+0022	J1058+0133
AS2UDS012.0	02:18:03.6	−04:55:27.2	2.520	02-03-2022	138.9	0.26	2.″6 × 2.″0, 87°	J0228–0337	J0238+1636
AS2UDS026.0	02:19:02.1	−05:28:56.9	3.296	01-03-2022	114.6	0.40	3.″2 × 2.″6, −78°	J0217–0820	J0238+1636
AS2UDS126.0	02:15:46.7	−05:18:49.2	2.436	02-03-2022	143.2	0.23	3.″0 × 1.″9, 72°	J0217–0820	J0238+1636
…	…	…	…	13-03-2022	…	…	…	…	J0423–0120
…	…	…	…	22-03-2022	…	…	…	…	J2258–2758

Note. Coordinates for the remaining nine sources in the full sample can be found in C.-C. Chen et al. (2022) and M. Frias Castillo et al. (2023).
[a] For channels of 60 km s^{-1}.

Table 2
Observed [C i], Co(1-0), mid-J CO and Dust Continuum Luminosities

Target	z	$I_{[C\,I]}$ (Jy km s^{-1})	FWHM$_{[C\,I]}$ (km s^{-1})	$L'_{[CI]}$ (10^{10} K km s^{-1} pc^2)	$M_{gas,[C\,I]}$ ($10^{10}M_\odot$)	$L'_{CO(1-0)}$ (10^{10} K km s^{-1} pc^2)	J_{up}	$L'_{CO(J_{up}-(J_{up}-1))}$ (10^{10} K km s^{-1} pc^2)	L_{IR} ($10^{12}L_\odot$)	S_{3mm} (mJy)
AS2COS0001.1	4.625	0.54 ± 0.20	680 ± 170	2.44 ± 0.91	9.9 ± 3.7	<19.8[f]	5	2.7 ± 0.6[c]	$36.3^{+5.0}_{-6.7}$	0.38 ± 0.04
AS2COS0002.1	4.595	0.39 ± 0.15	⋯	1.75 ± 0.67	7.1 ± 2.7	<20.8[f]	5	3.8 ± 0.8[c]	$9.5^{+3.1}_{-2.9}$	0.22 ± 0.03
AS2COS0008.1	3.581	1.03 ± 0.14	700 ± 90	3.12 ± 0.42	12.7 ± 1.7	11.6 ± 3.9[b]	4	5.2 ± 0.6[c]	$15.9^{+0.2}_{-1.1}$	0.40 ± 0.03
AS2COS0009.1	2.260	<0.42	840 ± 350	<0.6	<2.3	< 6.4[b]	3	8.4 ± 1.2[c]	$4.4^{+0.8}_{-0.1}$	0.58 ± 0.04
AS2COS0014.1	2.921	0.76 ± 0.35	750 ± 160	1.65 ± 0.76	6.7 ± 3.1	9.1 ± 3.4[f]	3	9.1 ± 1.5[c]	$10.7^{+0.7}_{-1.0}$	0.62 ± 0.03
AS2COS0023.1	4.341	0.70 ± 0.14	480 ± 80	2.87 ± 0.57	11.6 ± 2.3	7.0 ± 3.1[b]	4	9.1 ± 0.7[c]	$20.4^{+0.7}_{-0.5}$	0.21 ± 0.03
AS2COS0044.1	2.580	<0.27	⋯	<0.47	<2.0	<13.3[f]	3	5.0 ± 0.6[c]	$3.1^{+0.6}_{-0.7}$	1.34 ± 0.02
AS2COS0065.1	2.414	1.44 ± 0.16	580 ± 50	2.27 ± 0.25	9.2 ± 1.0	<13.2[f]	3	8.1 ± 0.8[c]	$9.3^{+0.9}_{-0.7}$	0.46 ± 0.02
AS2COS0066.1[g]	3.247	0.61 ± 0.29	160 ± 50	1.45 ± 0.36	5.6 ± 1.5	4.9 ± 2.5[f]	4	3.7 ± 0.4[c]	$6.8^{+0.9}_{-0.9}$	0.23 ± 0.03
AS2UDS012.0	2.520	0.72 ± 0.26	740 ± 140	1.22 ± 0.44	5.0 ± 1.8	11.1 ± 2.3[b]	3	4.0 ± 0.8[d]	$4.3^{+0.1}_{-0.1}$	0.32 ± 0.03
AS2UDS026.0	3.296	0.99 ± 0.31	700 ± 150	2.63 ± 0.82	10.6 ± 3.3	6.3 ± 2.9[b]	4	4.3 ± 0.8[d]	$4.5^{+0.8}_{-0.9}$	0.19 ± 0.02
AS2UDS126.0	2.436	1.17 ± 0.19	680 ± 70	1.87 ± 0.30	7.6 ± 1.2	4.9 ± 2.9[b]	3	4.3 ± 0.8[d]	$9.3^{+2.6}_{-1.9}$	0.43 ± 0.02
AS2COS0011.1	4.78	1.1 ± 0.3[c]	640 ± 60	5.1 ± 1.7	20.7 ± 6.9	<35[a]	5	6.7 ± 0.8[c]	$12.6^{+2.6}_{-2.3}$	0.47 ± 0.02
AS2COS0031.1	3.64	1.0 ± 0.2[c]	400 ± 60	3.1 ± 0.7	12.6 ± 2.8	12.7 ± 3.5[b]	4	8.9 ± 0.7[c]	$14.8^{+0.3}_{-0.3}$	0.28 ± 0.02
AS2UDS011.0	4.07	0.73 ± 0.24[d]	610 ± 220	2.7 ± 0.9	10.9 ± 3.6	4.7 ± 2.7[b]	4	3.9 ± 1.0[d]	$11.8^{+1.6}_{-2.0}$	0.12 ± 0.02
AS2UDS014.0[h]	3.8	0.23 ± 0.36[d]	1560 ± 5	<3.6	<14.6	<15.2[b]	4	9.9 ± 1.2[d]	$8.7^{+1.9}_{-0.2}$	0.19 ± 0.03
CDFN2	4.42	0.90 ± 0.10[e]	500 ± 50	3.79 ± 0.4	15.4 ± 1.6	12.9 ± 3.8[b]	4	8.2 ± 0.3[e]	$17.0^{+0.8}_{-0.5}$	0.35 ± 0.03
CDFN8	4.14	0.61 ± 0.12[e]	650 ± 70	2.32 ± 0.44	9.4 ± 1.8	7.0 ± 4.3[b]	4	4.6 ± 0.3[e]	$8.0^{+1.8}_{-1.2}$	0.20 ± 0.04
AEG2	3.67	0.70 ± 0.13[e]	830 ± 80	2.21 ± 0.39	9.0 ± 1.6	11.4 ± 3.4[b]	4	4.4 ± 0.2[e]	$5.8^{+0.1}_{-0.1}$	0.23 ± 0.04
AEG3	4.05	0.35 ± 0.07[e]	600 ± 70	1.29 ± 0.22	5.2 ± 0.9	<6.0[b]	4	2.7 ± 0.2[e]	$6.9^{+2.7}_{-1.2}$	0.11 ± 0.03

Notes. Individual columns list: galaxy ID; spectroscopic redshift; total [C i](1–0) flux density; line width; line luminosity; gas masses inferred from [C i](1–0) using $X_{[C\,I]} = 5.1 \times 10^{-5}$; CO(1–0) line luminosity; available mid–J CO transition; mid-J CO line luminosity; far-infrared luminosity; continuum flux density for the SMGs studied in this work. We consider sources with a peak SNR $\geqslant 2$ to be a detection. Sources below the solid line are published [C I](1–0) observations (J. E. Birkin et al. 2021; C.-C. Chen et al. 2022, and A. Huber 2025, in preparation) that we include in this work with their corresponding new CO(1–0) observations.
[a] We downloaded and calibrated the data from the NRAO archive, project 21A-254 (P.I.: Hodge). Fluxes were calculated following M. Frias Castillo et al. (2023). Line luminosities taken from:
[b] M. Frias Castillo et al. (2023).
[c] C.-L. Liao et al. (2024).
[d] J. E. Birkin et al. (2021).
[e] A. Huber 2025, in preparation.
[f] Hodge, J. priv. comm.
[g] AS2COS0066.1 falls on the edge of the ALMA Band, so we only cover the velocity range spanned by the main component of the emission seen in CO(4–3) (C.-C. Chen et al. 2022). This component represents ∼75% of the total flux, so we scale the inferred CO(1–0) luminosity down by 25%, and note that this measurement is a lower limit of the total [C I] line flux.
[h] Although AS2UDS014.0 is reported as a detection in J. E. Birkin et al. (2021), it does not pass our 2σ criterion for a detection. Therefore, we take three times the reported error on the line luminosity as an upper limit for this source.

and S. Berta et al. (2023).[31] We exclude galaxies classified as active galactic nuclei (AGN) according to F. Valentino et al. (2020), and we restrict our compilation to only sources with either CO(1–0) or CO(2–1) observations to minimize the uncertainty introduced by excitation corrections. The literature data with mid–J_{up} CO observations have been converted to CO(1–0) using $r_{21} = /L'_{CO(1-0)} = 0.9$ (J. E. Birkin et al. 2021). When necessary, fluxes and luminosities of the literature sources have been corrected for magnification. Although the SMGs in this work are marginally above the $L'_{[CI](1-0)}$–L_{IR} relation found for other ULIRGs and main-sequence galaxies (F. Valentino et al. 2018), they are mostly within the 0.26 dex scatter of the relation (we assess whether our sample could be drawn from the $L'_{[CI](1-0)}$–L_{IR} relation from F. Valentino et al. (2018) using a χ^2 test and find a p–value =0.7, consistent with being drawn from the same distribution).

As shown in Figure 2 (left) and Table 2, we do not detect [C I] emission in two sources, AS2COS0009.1 and AS2COS00044.1. Their 3σ upper limits fall within the $L'_{[C1]](1-0)}$–L_{IR} relation, so it is possible that they are too gas-poor to be detected given the sensitivity of our data.

The right panel of Figure 2 shows the $L'_{[CI]](1-0)}/L'_{CO(1-0)}$ ratio as a function of redshift. We calculate a median ratio of $\log(L'_{[CI](1-0)}/L'_{CO(1-0)}) = -0.62 \pm 0.14$, comparable with the value for the high-redshift SMG literature sample and the local ULIRGs (-0.74 ± 0.12). This ratio is also consistent with the value of $\log(L'_{[CI](1-0)}/L'_{CO(2-1)}) = (-0.69 \pm 0.04)$ found by F. Valentino et al. (2018). The $z \sim 1$ main-sequence galaxies have a lower median value (-0.85 ± 0.16), although it is still consistent with our sample. We also find no difference in $L'_{[CI](1-0)}/L'_{CO(1-0)}$ ratios when compared to total L_{IR}. Therefore, [C I](1–0) and CO(1–0) appear to be

[31] S. Berta et al. (2023) do not classify their targets as MS or SMG, and they do not report whether they are magnified. Given their large L_{IR}, we conservatively consider them lensed SMGs.

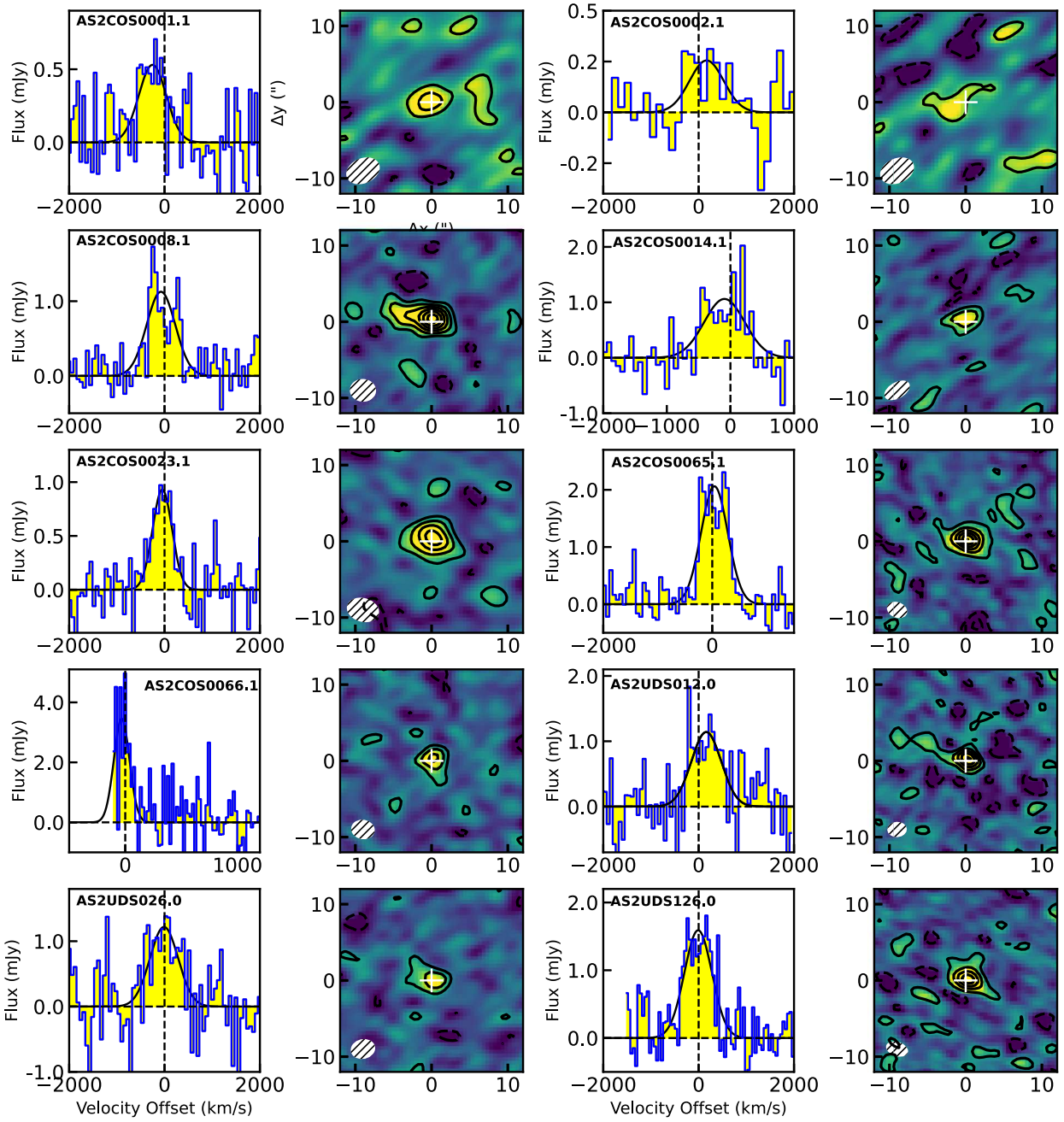

Figure 1. [C I](1–0) line emission for the detections in our sample of SMGs. The spectra (blue line and yellow fill, left panels) are extracted within a 2.″5 radius aperture to maximize the SNR. The spectra were fit with a single-Gaussian model allowing for a varying line width, shown by the black curve. The zeroth-moment maps (right panels) were collapsed over a velocity range equal to the FWHM of the respective mid–J_{up} CO emission line and show a 20″ × 20″ field of view. The systemic velocity is based on the redshift derived from the mid–J_{up} CO lines. The white cross indicates the peak of the mid–J_{up} CO line emission. Contours start at 2σ and increase in steps of 2σ, except for AS2COS0065.1 and AS2UDS126.0, where they do so in steps of 4σ. The white ellipse shows the FWHM of the beam for each source.

correlated on global scales regardless of galaxy type, L_{IR}, and redshift.

3.2. Photodissociation Region Modeling

How do the physical conditions (density, UV irradiation) of the ISM in our sample compare to other high- and low-redshift galaxies? To answer this question, we use photodissociation region (PDR) modeling of the CO, [C I], and infrared continuum data available for our sources. For our analysis, we use the PDRTOOLBOX (M. J. Kaufman et al. 2006; M. W. Pound & M. G. Wolfire 2008) suite of 1D, semi-infinite slab models with constant density. These models solve simultaneously for the chemistry, thermal balance, and radiative transfer, assuming metal, dust, and polycyclic aromatic hydrocarbons abundances, and a gas microturbulent velocity dispersion. For each combination of properties, every model is described in terms of the (number) density of H nuclei (n [cm^{-3}]) and the intensity of the incident far-ultraviolet radiation (G_{UV}, in units of the local interstellar field $G_0 = 1.6 \times 10^{-3}$ erg cm^{-2} s^{-1}, H. J. Habing 1968).

For the PDR modeling, we consider the [C I](1–0), CO(1–0), mid-J CO, and L_{IR}. The CMB heating is not

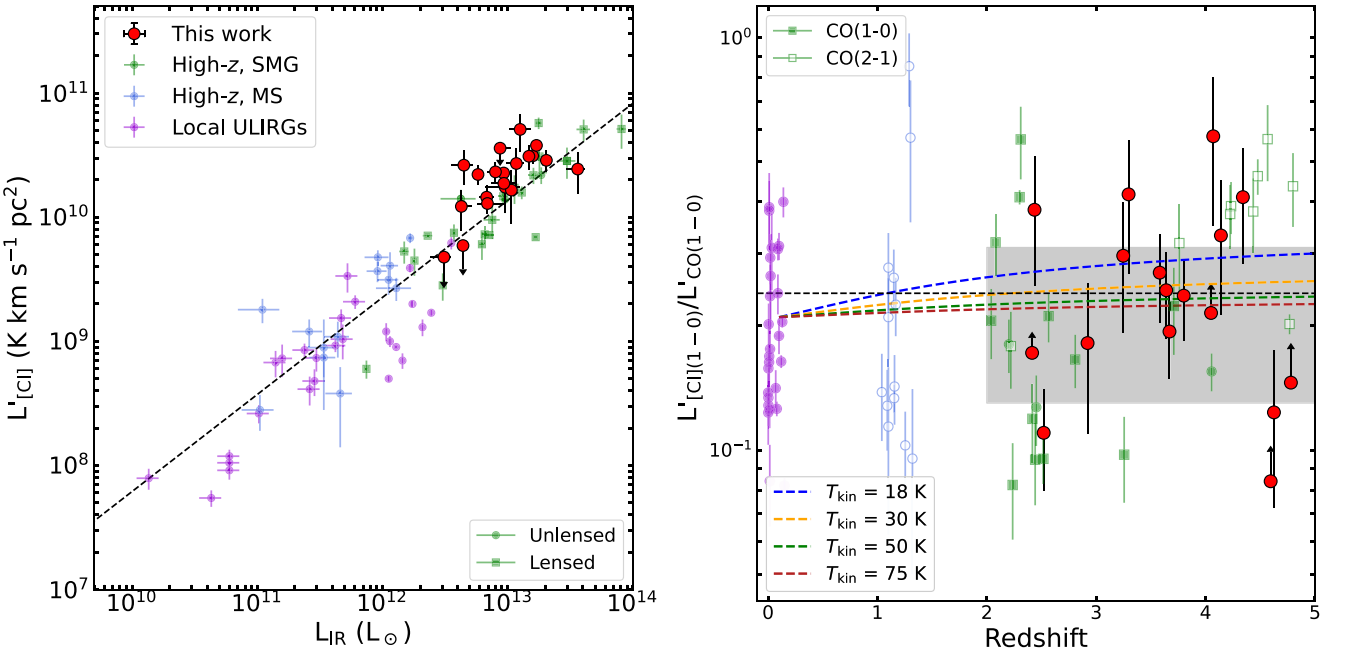

Figure 2. Left:[C I](1–0) line luminosities compared to $L_{\rm IR}$ for our sample. As comparison, we have added the local ULIRGs from D. Liu et al. (2019), J. Kamenetzky et al. (2016) and I. Montoya Arroyave et al. (2023), the $z \sim 1$ main-sequence galaxies from F. Valentino et al. (2018), G. Popping et al. (2017), S. Jin et al. (2019) and L. A. Boogaard et al. (2020), and the SMGs from F. Walter et al. (2011), S. Alaghband-Zadeh et al. (2013), M. S. Bothwell et al. (2017), R. Cañameras et al. (2018), N. P. H. Nesvadba et al. (2019), K. C. Harrington et al. (2018), H. Dannerbauer et al. (2019). We exclude galaxies classified as AGN according to F. Valentino et al. (2020). Literature luminosities are corrected for lensing magnification where necessary. The dashed line shows the best-fit relation from F. Valentino et al. (2018). Right: $L'_{[\rm CI](1-0)}/L'_{\rm CO(1\text{-}0)}$ ratio as a function of redshift. The dashed black line shows the median value for our sample, $\log\left(L'_{[\rm CI](1-0)}/L'_{\rm CO(1\text{-}0)}\right) = -0.72$, and the shaded region marks the absolute deviation around the median (0.14 dex). The dashed colored lines show the expected change in the ratio with redshift due to the warmer CMB for $n_{\rm H_2} = 10^2$ cm^{-3} and a range of gas kinetic temperatures (see Section 3.4).

implemented in the PDRTOOLBOX. We compare the data to default solar-metallicity PDRTOOLBOX models, which we consider to be a good "default" scenario for dusty SMGs (see Section 4). As the PDRTOOLBOX models consider only a single illuminated cloud face, we need to implement corrections for the optically thin tracers (in our case, IR continuum) and [C I] which will emit from both the near and far side of the clouds, whereas optically thick tracers (CO) will only be seen from the near side of the cloud. Namely, for the IR continuum and [C I], we multiply the predicted fluxes by a factor of 2.

The [C I](1–0)/$L_{\rm IR}$ and CO(1–0)/$L_{\rm IR}$ ratio, with [C I] and CO tracing the extended gas mass and $L_{\rm IR}$ tracing the SFR, allows us to constrain $G_{\rm UV}$. On the other hand, the ratio of [C I](1–0) or CO(1–0) and a mid–$J_{\rm up}$ CO line effectively traces the gas density, while being almost insensitive to $G_{\rm UV}$. We thus use a combination of these ratios to determine the PDR properties for this sample of SMGs. Where appropriate, we use the 3σ upper/lower limits. We repeat the process, excluding the CO(1–0) line: the results do not change appreciably except for AS2COS0009.1 ($G_{\rm UV}$ increases by 0.8 dex), AS2UDS12.0 (n increases by 0.5 dex), and AS2UDS126.0 ($G_{\rm UV}$ increases by $\sim$2 dex). For a consistent comparison, we take the luminosities of the comparison sample and calculate the densities and radiation field strengths.

We show the results of the PDR modeling in Figure 3 and Table 3. We homogenize the literature sample from Figure 2 by repeating the PDR fitting procedure with the same optical depth corrections. The SMGs show fairly high densities, with a median $n = 10^{4.7}$ cm^{-3} and a standard deviation of 0.2 dex. The UV radiation field has a median value of $G_{\rm UV} = 10^{3.2}$ G_0,

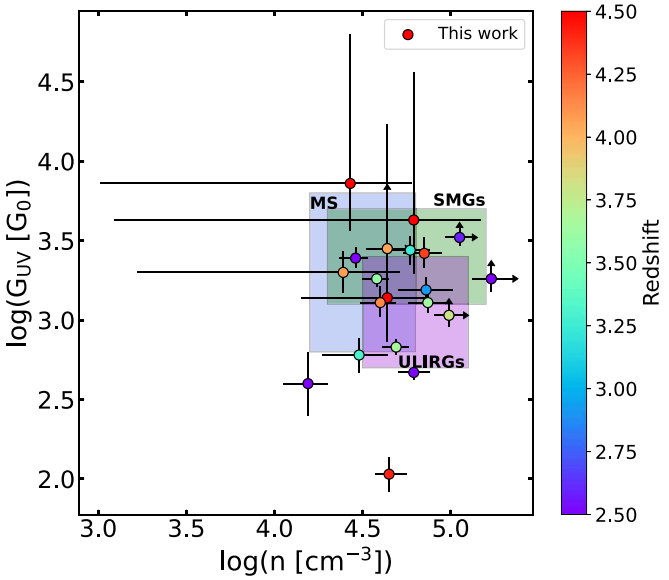

Figure 3. ISM density (n) and UV radiation field ($G_{\rm UV}$) derived from PDR modeling for the sample in this work. Our sources are denoted by the circles and color coded by redshift. We compare to the literature sample from Figure 2 with available [C I](1–0), mid $-$ $J_{\rm up}$ CO, and far-infrared data. Overall, our galaxies span the same parameter space as other sources at high redshift, with a median $n = 10^{4.7\pm0.2}$ cm^{-3} and a median UV radiation field of $G_{\rm UV} = 10^{3.2\pm0.4}$ G_0. The large scatter in $G_{\rm UV}$ likely reflects the varied nature of the sources studied in this work.

with a standard deviation of 0.4 dex. While $G_{\rm UV}$ and n likely vary significantly across individual galaxies (see, e.g., the resolved study of SDP.81 by M. Rybak et al. 2020), overall,

Table 3
Results of Photodissociation Region Modeling for Individual Sources

Target	G_{UV} (log G_0)	n_{H_2} (log cm^{-3})
AS2COS0001.1	$3.86^{+0.94}_{-0.30}$	$4.43^{+0.35}_{-1.42}$
AS2COS0002.1	$3.63^{+0.93}_{-0.34}$	$4.79^{+0.38}_{-1.70}$
AS2COS0008.1	$3.26^{+0.05}_{-0.05}$	$4.58^{+0.07}_{-0.08}$
AS2COS0009.1	$3.26^{+0.04}_{-0.05}$	$5.23^{+0.12}_{-0.11}$
AS2COS0014.1	$3.19^{+0.08}_{-0.09}$	$4.86^{+0.15}_{-0.16}$
AS2COS0023.1	$3.42^{+0.10}_{-0.09}$	$4.85^{+0.10}_{-0.12}$
AS2COS0044.1	$3.52^{+0.06}_{-0.05}$	$5.05^{+0.07}_{-0.08}$
AS2COS0065.1	$3.39^{+0.07}_{-0.06}$	$4.46^{+0.07}_{-0.09}$
AS2COS0066.1	$3.44^{+0.09}_{-0.09}$	$4.77^{+0.11}_{-0.13}$
AS2UDS012.0	$2.67^{+0.05}_{-0.05}$	$4.79^{+0.09}_{-0.09}$
AS2UDS026.0	$2.78^{+0.11}_{-0.11}$	$4.48^{+0.16}_{-0.21}$
AS2UDS126.0	$2.60^{+0.20}_{-0.20}$	$4.19^{+0.11}_{-0.14}$
AS2COS0011.1	$3.14^{+1.09}_{-0.28}$	$4.64^{+0.23}_{-0.49}$
AS2COS0031.1	$3.11^{+0.06}_{-0.06}$	$4.87^{+0.10}_{-0.11}$
AS2UDS011.0	$3.30^{+0.13}_{-0.13}$	$4.39^{+0.19}_{-0.29}$
AS2UDS014.0	$3.03^{+0.07}_{-0.07}$	$4.99^{+0.08}_{-0.08}$
CDFN2	$2.03^{+0.11}_{-0.11}$	$4.65^{+0.07}_{-0.08}$
CDFN8	$3.11^{+0.10}_{-0.09}$	$4.60^{+0.09}_{-0.11}$
AEG2	$2.83^{+0.05}_{-0.05}$	$4.69^{+0.07}_{-0.08}$
AEG3	$3.45^{+0.37}_{-0.18}$	$4.64^{+0.10}_{-0.12}$

Note. We list inferred G_{UV} and n_{H_2} values.

SMGs in our sample occupy a similar parameter space as the main-sequence galaxies, as well as other high-redshift SMGs. The large spread in G_{UV} reflects the varied nature of the SMGs in our sample, as indicated by the wide range of CO excitation (i.e., CO(3–2)/CO(1–0) ratios spanning more than 1 dex; M. Frias Castillo et al. 2023).

3.3. Comparison between Molecular Gas Tracers

We now cross–calibrate CO(1–0), [C I](1–0), and dust continuum as gas mass tracers and test their agreement. Figure 2 (right) shows that the SMGs in this work follow the correlation between CO(1–0) and [C I](1–0) line luminosities seen at low redshift (e.g., Q. Jiao et al. 2017, 2019; I. Montoya Arroyave et al. 2023), at least when averaged over global scales. This relation, along with the similarity in FWHM of the line profiles, suggests that the line emission from both lines arises from similar volumes in the galaxy and has been one of the main arguments for the use of [C I] as a molecular gas tracer.

The absolute values of the light-to-mass conversion factors for [C I] and CO(1–0) have been the subject of extensive study in the literature. For [C I], the conversion is directly dependent on the assumed carbon abundance, $X_{[C\,I]}$, which varies with metallicity (K. E. Heintz & D. Watson 2020). $X_{[C\,I]}$ estimates in the literature range from $\sim 1–2 \times 10^{-5}$ for MS galaxies (F. Valentino et al. 2018; Q. Jiao et al. 2019; L. A. Boogaard et al. 2020) to $\sim 4–8 \times 10^{-5}$ for ULIRGs and SMGs (F. Walter et al. 2011; S. Alaghband-Zadeh et al. 2013; M. S. Bothwell et al. 2017; Q. Jiao et al. 2017; G. Gururajan et al. 2023). CO(1–0), on the other hand, relies on the choice of α_{CO}, which also depends on metallicity, turbulence, and gas kinematics (A. D. Bolatto et al. 2013). Empirical calibrations for α_{CO} derive values from $\sim 0.8–1\ M_\odot\ (\mathrm{K\,km\,s^{-1}\,pc^2})^{-1}$ for local ULIRGs and some SMGs (e.g., D. Downes & P. M. Solomon 1998; A. L. R. Danielson et al. 2011; P. P. Papadopoulos et al. 2012; C.-C. Chen et al. 2017; G. Calistro Rivera et al. 2018; J. E. Birkin et al. 2021; A. Amvrosiadis et al. 2023) to $\sim 3–5\ M_\odot\ (\mathrm{K\,km\,s^{-1}\,pc^2})^{-1}$ for local disks and main-sequence galaxies at high redshift (K. M. Sandstrom et al. 2013; Q. Remy et al. 2017; D. Cormier et al. 2018; L. Dunne et al. 2022).

3.3.1. [C I](1–0) Line Emission as a Gas Mass Tracer

Following P. P. Papadopoulos & T. R. Greve (2004) and L. Dunne et al. (2022), we calculate the total molecular gas mass from the [C I] line luminosity using the following expression:

$$M_{H_2}^{[CI]} = \frac{0.0127}{X_{[CI]}\,Q_{10}} \left(\frac{D_L^2}{1+z}\right) I_{[CI](1-0)}\ M_\odot, \tag{3}$$

or in terms of line luminosity:

$$M_{H_2}^{[CI]} = \frac{9.51 \times 10^{-5}}{X_{[CI]}\,Q_{10}}\, L'_{[CI](1-0)}\ M_\odot, \tag{4}$$

where $X_{[C\,I]}$ is the C/H_2 abundance ratio and Q_{10} is the [C I] excitation factor of the [C I] $J = 1 \rightarrow 0$ level. The value of Q_{10} is straightforward to calculate under the assumption of local thermodynamic equilibrium (LTE):

$$Q(T_{ex}) = 3e^{(-T_1/T_{ex})}/(1 + 3e^{(-T_1/T_{ex})} + 5e^{(-T_2/T_{ex})}), \tag{5}$$

where $T_1 = 23.6$ K and $T_2 = 62.5$ K are the excitation energy levels of atomic carbon. We adopt a typical value of $T_{ex} = 30$ K (A. Weiß et al. 2003; F. Walter et al. 2011; K. C. Harrington et al. 2021), which results in $Q_{10} = 0.46$. We note that, above $T_{ex} \sim 20$ K, the derived carbon masses depend very weakly on the assumed temperature (A. Weiß et al. 2005). P. Papadopoulos et al. (2022) found however that the [C I] lines are subthermally excited in the ISM of galaxies, which means that Q_{10} becomes a nontrivial function of density and temperature. Our choice of $T_{ex} = 30$ K and LTE only implies a 4% higher mass compared to more complex non-LTE approaches (K. C. Harrington et al. 2021; L. Dunne et al. 2022; P. Papadopoulos et al. 2022), which is negligible compared to the uncertainty in $X_{[C\,I]}$.

We obtain the CO(1–0)–based molecular gas masses following the standard equation:

$$M_{H_2}^{CO} = \alpha_{CO}\, L'_{CO(1-0)}\ M_\odot, \tag{6}$$

where α_{CO} is the CO-to-H_2 conversion factor, which we take to be $1\ M_\odot\ (\mathrm{K\,km\,s^{-1}\,pc^2})^{-1}$ (e.g., A. L. R. Danielson et al. 2011; J. A. Hodge et al. 2012; C. De Breuck et al. 2014; C.-C. Chen et al. 2017; G. Calistro Rivera et al. 2018; R. Xue et al. 2018; D. A. Riechers et al. 2020b; M. Frias Castillo et al. 2022; A. Amvrosiadis et al. 2023).

Combining Equations (4) and (6), we can constrain the product of the two main unknowns for each tracer (for $Q_{10} = 0.46$):

$$X_{[CI]} \times \alpha_{CO} = 2.07 \times 10^{-4} \frac{L'_{[CI]}}{L'_{CO}}. \tag{7}$$

In Figure 4 we show $X_{[C\,I]} \times \alpha_{CO}$ as a function of redshift and L_{IR}, color coded by the intensity of the far-ultraviolet (FUV) radiation field, G_{UV}. We do not show the sources where neither CO(1–0) nor [C I](1–0) are detected. The factor does not appear to be correlated with G_{UV}, suggesting that it could

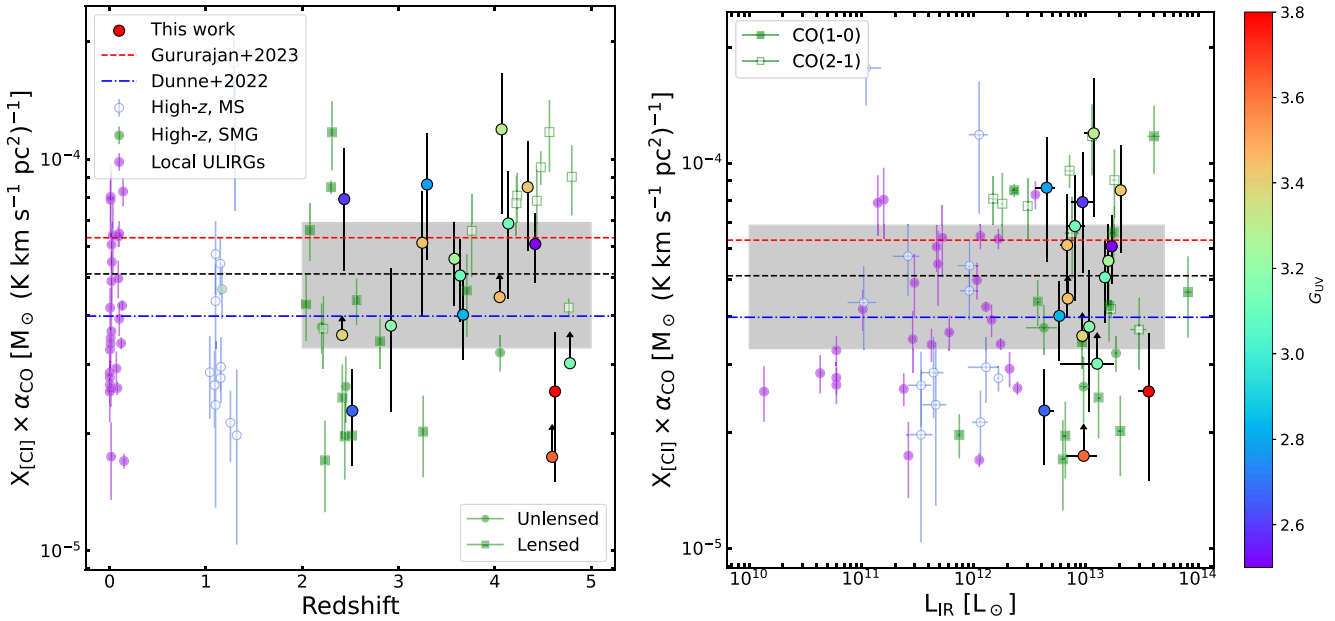

Figure 4. $X_{[C\,I]} \times \alpha_{CO}$ factor as a function of redshift (left) and L_{IR} (right) for our sample. Our sample is shown in circles, color coded by their FUV radiation field. The literature compilation is as indicated in Figure 2. The mean value for the sample in this work is shown as a black dashed line, and the gray-shaded region represents the 1σ standard deviation around the sample mean, $(4.5 \pm 2.0) \times 10^{-5}$ (K km s^{-1} pc^2)$^{-1}$. The dashed lines mark the mean values from G. Gururajan et al. (2023) and L. Dunne et al. (2022). We fit the full sample to look for trends with either parameter, but do not find any dependence of $X_{[C\,I]} \times \alpha_{CO}$ on either redshift or L_{IR}. The lack of correlation with G_{UV} suggests that $X_{[C\,I]} \times \alpha_{CO}$ is also insensitive to local conditions of the ISM in our sample.

be insensitive to local conditions of the ISM in our sample. We look for any trends in the sample with LINMIX (B. C. Kelly 2007), a Bayesian linear regression fitting model that can fit data with errors along with the upper limits. Our fits return a slope of 0.02 ± 0.02 and 0.01 ± 0.05 for the dependence on redshift and L_{IR}, respectively. The full sample has a scatter of 0.12 dex in both cases. This is consistent with no dependence on either parameter, and we can thus compute a constant conversion factor. We find a median $X_{[C\,I]} \times \alpha_{CO} = (5.1 \pm 1.8) \times 10^{-5}\ M_\odot$ (K km s^{-1} pc^2)$^{-1}$ and a mean $(5.4 \pm 2.6) \times 10^{-5}\ M_\odot$ (K km s^{-1} pc^2)$^{-1}$ for the galaxies in our sample (not including those with both CO and [C I] nondetections).

3.3.2. Dust Continuum Emission as a Gas-Mass Tracer

Because the Rayleigh–Jeans (RJ) tail of the dust emission is almost always optically thin, it can trace the total dust mass, and therefore potentially the molecular gas mass, provided that the dust emissivity per unit mass and the dust-to-gas abundance ratio can be constrained. Under the assumption of a mass-weighted cold dust temperature, T_{dust} (25 K is typically considered to be representative for both local star-forming and high-redshift galaxies), and a dust emissivity index, β (generally taken to be 1.8), the CO(1–0) luminosity and rest-frame 850 μm continuum flux have been shown to correlate for a range of galaxy populations (e.g., N. Scoville et al. 2016 for local SFGs, ULIRGs and high-redshift SMGs, and M. Kaasinen et al. 2019 for $z \sim 2$ SFGs). From a single-band continuum flux measurement, the $L_{850\ \mu m,rest}$ can be calculated following N. Scoville et al. (2016, 2017):

$$L_{850\mu m,rest} = 1.19 \times 10^{27} S_{\nu_{obs}} (1+z)^{-(3+\beta)} \times \left(\frac{\nu_{850}}{\nu_{obs}}\right)^{2+\beta} D_L^2 \frac{\Gamma_0(T_{dust})}{\Gamma_{RJ}(T_{dust}, z)}\ \text{erg s}^{-1}\,\text{Hz}^{-1}, \quad (8)$$

where ν_{obs} is the observed-frame frequency where the continuum flux density is measured and Γ_{RJ} is the correction for departures in the rest frame of the Planck function from Rayleigh–Jeans. The H_2 mass is then obtained via:

$$M_{H_2}^{dust} = \frac{L_{850\ \mu m,rest}}{\alpha_{850}} M_\odot, \quad (9)$$

where α_{850} is the luminosity-to-gas mass conversion factor for dust at rest-frame 850 μm. The 3 mm dust-continuum emission measurements for our sample probe rest-frame wavelengths in the range $\lambda_{rest} \sim 650$–$520\ \mu$m, so we calculate the extrapolated $L_{850\mu m,rest}$ and compare them against the CO and [C I] line luminosities to constrain the product of their conversion factors. First, we need to make an assumption for T_{dust} and β. Studies on the dust SED of SMGs find that they are characterized by warmer temperatures and steeper β (e.g., A. Saintonge et al. 2013; E. da Cunha et al. 2021; L. Dunne et al. 2022; S. Jin et al. 2022; C.-L. Liao et al. 2024) than the typically assumed $T_{dust} = 25$ K and $\beta = 1.8$. Following C.-L. Liao et al. (2024), who performed SED fitting with CIGALE for a subsample of the sources in this work, we set $T_{dust} = 30$ K and $\beta = 2.1$ and calculate $L_{850\ \mu m,rest}$. If we had chosen $T_{dust} = 25$ K and $\beta = 1.8$ instead, the luminosities would have been 15% higher.[32]

In Figure 5 we show the distribution of $\alpha_{CO} \times \alpha_{850}$ and $X_{[C\,I]}/\alpha_{850}$ for our sample as a function of redshift. We fit the distributions again using LINMIX. In all cases, the fits have a slope consistent with no trend with either parameter, so we

[32] While the choices of T_{dust} and β have a relatively minor effect on the derived $L_{850\ \mu m,rest}$ from the observed-frame 3 mm dust continuum, the impact becomes more severe if the observed wavelength does not probe the RJ tail of the dust emission. If we had used observed-frame 850 μm dust-continuum observations, which are more commonly available at high redshift, the derived luminosities could have been overestimated by more than 50%.

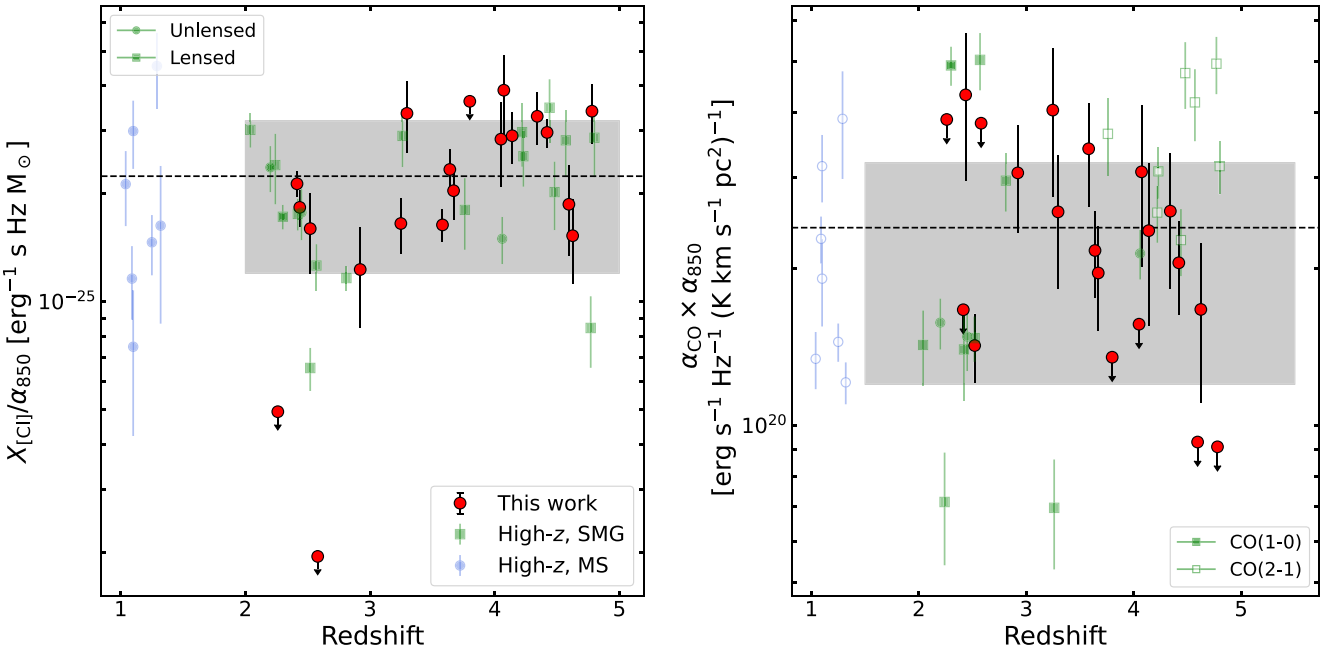

Figure 5. $X_{[C\,I]}/\alpha_{850}$ (left) and $\alpha_{CO} \times \alpha_{850}$ (right) factors as a function of redshift for our sample. The mean value for the sample in this work is shown as a black dashed line, and the gray-shaded region represents the 1σ standard deviation around the sample mean. For comparison, we show the $z \sim 1$ MS galaxies from ASPECS (L. A. Boogaard et al. 2020) and high-redshift SMGs (F. Walter et al. 2011; S. Alaghband-Zadeh et al. 2013; M. S. Bothwell et al. 2017; R. Cañameras et al. 2018; K. C. Harrington et al. 2018; N. P. H. Nesvadba et al. 2019). We do not find evidence for any trends with redshift or L_{IR} (not shown) for either pair.

compute a mean constant conversion factor for the whole sample of:

$$\alpha_{CO} \times \alpha_{850} = \frac{L_{850\,\mu m,rest}}{L'_{CO}}$$
$$= (2.4 \pm 1.0) \times 10^{20}\ \mathrm{erg\ s^{-1}\ Hz^{-1}\ (K\ km\ s^{-1}\ pc^2)^{-1}}$$

$$X_{[CI]}/\alpha_{850} = 2.07 \times 10^{-4} \frac{L'_{[CI]}}{L_{850\,\mu m,rest}}$$
$$= (2.2 \pm 1.0) \times 10^{-25}\ (\mathrm{erg\ s^{-1}\ Hz^{-1}})^{-1}.$$

3.4. Cosmic Microwave Background Effect on CO and [C I] Emission at High Redshift

Our sample of SMGs spans a redshift range ~2–5. Therefore, it is important to consider the effect that the CMB will have on the recoverable emission of the ground-state transitions for both CO and [C I], as its temperature increases (E. da Cunha et al. 2013; Z.-Y. Zhang et al. 2016). We model how the measured CO(1–0) and [C I](1–0) intensities, as well as their ratio, vary with increasing T_{CMB} for a range of gas densities and kinetic temperatures, and we show the results in Figure 6. We use RADEX (F. F. S. van der Tak et al. 2007) for the models, a non-LTE radiative transfer code which uses the escape probability method, and we take collisional data between each molecule and H_2 from the LAMBDA database (F. L. Schöier et al. 2005). We fix the H_2 ortho—to—para ratio to 3:1 and set $\log(N_{CO}/dv) = \log(N_C/dv) = 18$.

Our models indicate a nonnegligible decrease in the recovered [C I](1–0) intensity for a given gas kinetic temperature and density. The magnitude of the effect is mostly determined by the kinetic temperature of the gas, with the density having barely any impact on the resulting emission. However, decreases in recovered line intensities for both CO(1–0) and [C I](1–0) offset each other, such that there is a negligible effect on the measured luminosity ratio for the warmer gas temperatures ($T_{kin} \geqslant 50$ K). For the colder temperatures, the ratio can decrease by up to ~30%. As a lower bound for the T_{kin} in our sample, we can consider the excitation temperature of the CO(1–0)-emitting layer from our PDR models; this is 18–20 K, though the real T_{kin} is likely significantly higher. Given the current scatter of the CO(1–0) and [C I](1–0) data, it is challenging to detect a suppression of this magnitude in the ratio. We perform the same analysis for dust emission (see Appendix), and find that the CO/dust and [C I]/dust flux ratios also stay approximately constant with redshift, as the effect of the CMB is of a similar order of magnitude for all tracers individually (assuming $T_{dust} = T_{kin} \sim 30$ K).

How would these effects impact the observed luminosity ratios? The warmer CMB background would act to increase the $X_{[C\,I]} \times \alpha_{CO}$ factor needed for higher-redshift sources. This is not immediately evident from Figure 4, as the fit to the data is consistent with no evolution with redshift. If we separate our sources into two bins at $z < 3.5$ and $z > 3.5$, we find consistent mean factors for both bins ($5.6 \pm 2.0 \times 10^{-5}$ $M_\odot$ (K km s^{-1} pc^2)$^{-1}$ versus $5.1 \pm 1.8 \times 10^{-5}$ $M_\odot$ (K km s^{-1} pc^2)$^{-1}$). This suggests that, at least out to $z \sim 5$, the ratio of both tracers is not obviously suppressed compared to that of local ULIRGs. This could be a selection effect, as we are currently restricted to the most massive, dusty, star-forming galaxies at higher redshifts, where gas temperatures and densities, as well as metallicities, are expected to be higher than in normal, main-sequence galaxies (F. Valentino et al. 2020; K. C. Harrington et al. 2021; S. Jarugula et al. 2021). We also caution that there is a larger spread in ratios for the high-redshift sources compared to the $z = 0$ ULIRGs. For the conversion factors involving dust, we find $1.5 \pm 1.0 \times 10^{-25}$ versus $2.7 \pm 1.0 \times 10^{-25}$ erg s^{-1} Hz^{-1} (K km s^{-1} pc^2)$^{-1}$ for $\alpha_{CO} \times \alpha_{850}$, and $1.8 \pm 0.8 \times 10^{20}$ versus $3.1 \pm 0.8 \times 10^{20}$ K km s^{-1} pc^2 (erg s^{-1} Hz^{-1})$^{-1}$

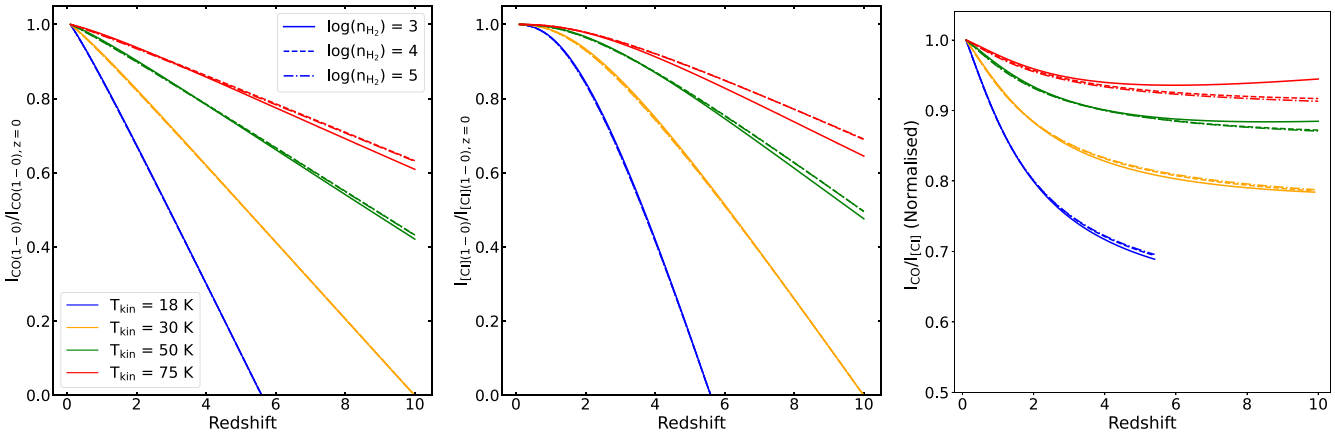

Figure 6. Recovered $I_{CO(1-0)}$ (left), $I_{[CI](1-0)}$ (middle), and their ratio (right) as a function of redshift. For each panel, we plot the measured intensity at each redshift divided by the intrinsic intensity measured at $z = 0$, where $T_{CMB} = 2.73$ K. We show three examples of H_2 density, $\log(n) = 3$, 4, and 5, as well as a range of gas kinetic temperatures, for a column density of $N_{CO,C}/dv = 10^{18}$ cm^{-2} km^{-1} s.

for $X_{[C\,I]}/\alpha_{850}$ for the lower and higher-redshift bins, respectively—again consistent with no evolution with redshift.

4. Discussion

The observations of CO(1–0) and [C I](1–0) presented here for a sample of dusty, star-forming galaxies at $z \sim 2$–5 obviate the need for excitation corrections, allowing us to directly confirm that the relation found in the local Universe remains in place for the ground-state transition of both species out to $z \sim 5$. This suggests that [C I] coexists with CO in the cold gas reservoirs of high-redshift galaxies and is therefore a good tracer of the total molecular gas mass. However, as we do not yet have a calibration of [C I] as a tracer of molecular gas mass fully independent of CO, we can only constrain the product $X_{[C\,I]} \times \alpha_{CO}$ and relate it to the choice of α_{CO}. We find a median $X_{[C\,I]} \times \alpha_{CO} = (5.1 \pm 1.8) \times 10^{-5}$ $M_\odot$ (K km s^{-1} pc^2)$^{-1}$ and a mean of $(5.4 \pm 2.6) \times 10^{-5}$ $M_\odot$ (K km s^{-1} pc^2)$^{-1}$ (without including three sources that are undetected in both lines). This mean product is consistent with the value found for the SPT lensed galaxies by G. Gururajan et al. (2023) of $(6.3 \pm 0.7) \times 10^{-5}$ $M_\odot$ (K km s^{-1} pc^2)$^{-1}$ and the value obtained in the study by L. Dunne et al. (2022) of $(3.98 \pm 0.19) \times 10^{-5}$ $M_\odot$ (K km s^{-1} pc^2)$^{-1}$, which included a compilation of published CO(1–0) and [C I](1–0) observations available at that time.

Assuming a Milky Way value of $\alpha_{CO} = 3.6$, we derive a median $X_{[C\,I]} = (1.4 \pm 0.5) \times 10^{-5}$, which would be in agreement with abundances derived for local (Q. Jiao et al. 2019) and $z \sim 1$ main-sequence galaxies (F. Valentino et al. 2018; L. A. Boogaard et al. 2020), as well as the samples from L. Dunne et al. (2022; $1.6^{+0.5}_{-0.4} \times 10^{-5}$) and S. Berta et al. (2023; $1.4 \pm 0.5 \times 10^{-5}$). On the other hand, if we adopt $\alpha_{CO} \sim 1$, as is common for high-redshift SMGs and local ULIRGs, we obtain a mean carbon abundance of $X_{[C\,I]} = (5.1 \pm 1.8) \times 10^{-5}$, higher than the commonly adopted value of 3×10^{-5} (A. Weiß et al. 2003; P. P. Papadopoulos & T. R. Greve 2004; M. S. Bothwell et al. 2017) or the values found for main-sequence galaxies. Higher carbon abundances have been derived for local ULIRGs (Q. Jiao et al. 2017, 2019) and high-redshift SMGs (F. Walter et al. 2011; S. Alaghband-Zadeh et al. 2013; G. Gururajan et al. 2023), although the latter have commonly targeted lensed sources and relied on $J_{up} > 2$ CO observations. These higher values can be caused by regions with higher cosmic ray ionization rates or stronger FUV radiation field (Figure 3), which would dissociate CO into [C I] (T. G. Bisbas et al. 2021). Higher carbon abundances could also be explained by galaxies having higher metallicities —we return to this point below.

Finally, assuming $X_{[C\,I]} = 5.1 \times 10^{-5}$ and $\alpha_{CO} = 1$, we derive consistent mean values for the dust conversion factor $\alpha_{850} = (2.2 \pm 1.0) \times 10^{20}$ erg s^{-1} Hz^{-1} $M_\odot^{-1}$ and $(2.4 \pm 1.0) \times 10^{20}$ erg s^{-1} Hz^{-1} $M_\odot^{-1}$, respectively. This is a factor of two lower than the mean value of $(4.4 \pm 1.1) \times 10^{20}$ erg s^{-1} Hz^{-1} $M_\odot^{-1}$ derived in N. Scoville et al. (2016; correcting their value for $\alpha_{CO} = 1$ and removing the helium contribution, as we are only dealing with M_{H_2}).

Previous studies reported a discrepancy between the H_2 masses derived from CO and [C I] observations (e.g., M. S. Bothwell et al. 2017; F. Valentino et al. 2018; I. Montoya Arroyave et al. 2023). This can be explained by the fact that these studies used a bimodal α_{CO} while keeping the carbon abundance constant for all galaxy populations ($X_{[C\,I]} = 3 \times 10^{-5}$), which naturally results in a mismatch in the derived H_2 masses. We show this effect in Figure 7, where we have compiled the carbon abundances reported in previous studies. When corrected to the same α_{CO}, the values of $X_{[C\,I]}$ show a fairly linear distribution with L_{IR} and redshift, as previously noted by L. Dunne et al. (2022). However, if we adopt different values for α_{CO} for different galaxy populations, studies that adopt a ULIRG-like value generally find higher carbon abundances than those that use a Milky Way value instead.

Although L. Dunne et al. (2022) argued for near-universal values of $X_{[C\,I]} = 1.6 \times 10^{-5}$ and $\alpha_{CO} = 3.6$ $M_\odot$ (K km s^{-1} pc^2)$^{-1}$, multiple high-resolution studies of gas kinematics in SMGs have noted the difficulty of reconciling such a high α_{CO} with the derived stellar and dynamical masses, consistently finding that $\alpha_{CO} \sim 1$ (and therefore $X_{[C\,I]} \sim 5 \times 10^{-5}$) is preferred for this population (e.g., A. L. R. Danielson et al. 2011; J. A. Hodge et al. 2012; C. De Breuck et al. 2014; C.-C. Chen et al. 2017; G. Calistro Rivera et al. 2018; R. Xue et al. 2018; D. A. Riechers et al. 2020b; J. E. Birkin et al. 2021; M. Frias Castillo et al. 2022; A. Amvrosiadis et al. 2023, see also G. E. Magdis et al. 2011 for a similar conclusion on the $z = 4.05$ SMG GN20 using dust constraints). Following K. E. Heintz & D. Watson (2020), the

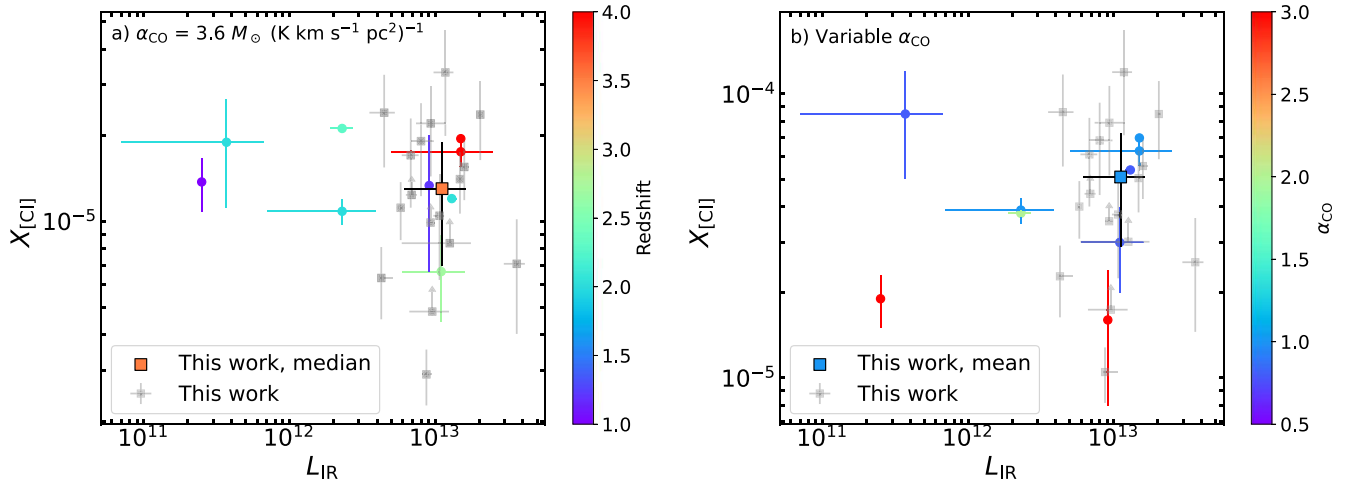

Figure 7. Left: values of $X_{[C\,I]}$ reported in the literature as a function of the average L_{IR} of the corresponding sample. We show the average of our sample and plot the individual points for each galaxy in gray. We show sources from A. L. R. Danielson et al. (2011), F. Walter et al. (2011), S. Alaghband-Zadeh et al. (2013), M. S. Bothwell et al. (2017), F. Valentino et al. (2018), H. Dannerbauer et al. (2019), L. A. Boogaard et al. (2020), N. P. H. Nesvadba et al. (2019), G. Gururajan et al. (2023), color coded by the average redshift of the sample. The values have been corrected for the same $\alpha_{CO} = 3.6$ (L. Dunne et al. 2022). Right: same as the panel on the left, but the points are color coded by the value of α_{CO} used to derive each carbon abundance. The introduction of a bimodal α_{CO} naturally leads to an equal bimodality in $X_{[C\,I]}$.

values of $X_{[C\,I]}$ derived for our sources assuming $\alpha_{CO} = 1$ would imply solar or supersolar metallicities (Figure 8).

This is in line with SMGs being dust enriched (S. Eales et al. 2024) and is consistent with recent results from rest-frame optical spectroscopy with Very Large Telescope's (VLT) KMOS (J. E. Birkin 2022, which includes SMGs from the AS2UDS and AS2COSMOS surveys) and JWST's NIRSpec (J. E. Birkin et al. 2023), although some SMGs might have subsolar metallicities (e.g., D. Rigopoulou et al. 2018; M. Rybak et al. 2023). This reaffirms our choice of α_{CO} and derived $X_{[C\,I]}$. Assuming $X_{[C\,I]} \sim 5 \times 10^{-5}$, we derive gas masses $M_{H_2,[CI]}$ in the range 5–21 $\times 10^{10} M_\odot$, consistent with $M_{H_2,CO} = 4$–$13 \times 10^{10} M_\odot$ using $\alpha_{CO} = 1$. Therefore, it is possible to obtain gas mass estimates from either tracer that agree within the uncertainties, so long as consistent assumptions are made when converting luminosities into gas masses. Finally, we note that, due to the relative brightness of [C I] compared to CO(1–0), [C I] will thus provide more precise gas mass estimates than CO(1–0) for the same integration time (though subject to the same systematic uncertainties).

The constant conversion factor that we have derived relies on the linear correlation between L'_{CO} and $L'_{[CI]}$ observed out to $z \sim 5$, as well as the lack of evolution of the ratio of both quantities with either redshift or L_{IR}. We have shown that the warmer CMB at higher redshifts has a moderate impact on the ratio, which can be suppressed by up to 30% for the lowest kinetic gas temperatures (Figure 6). In Figure 2 (right), we show the impact that this could have on the measured ratio at high redshift. We have taken the mean value of the line luminosity ratio $L'_{[CI]}/L'_{CO}$ for local ULIRGs (0.21) as the intrinsic value that an SMG would have at $z = 0$, and applied the correction for the effect of the CMB for different T_{kin}. The effect on the ratio is too small to be differentiated from the current scatter of the data, which is likely driven by the uncertainties in the measurements as well as the internal conditions of individual galaxies (G. Gururajan et al. 2023). We caution that this only applies to the ratio of both tracers, and that the CMB effect can be significant on individual lines, which in turn affects the absolute value of the molecular gas masses that we obtain at high redshift. In order to determine the absolute decrease of the line intensities due to the CMB of individual lines, it will be necessary to obtain more complete SLEDs to perform complex, non-LTE modeling of the gas excitation conditions (K. C. Harrington et al. 2021) and extend the sample to galaxies of lower mass and metallicities.

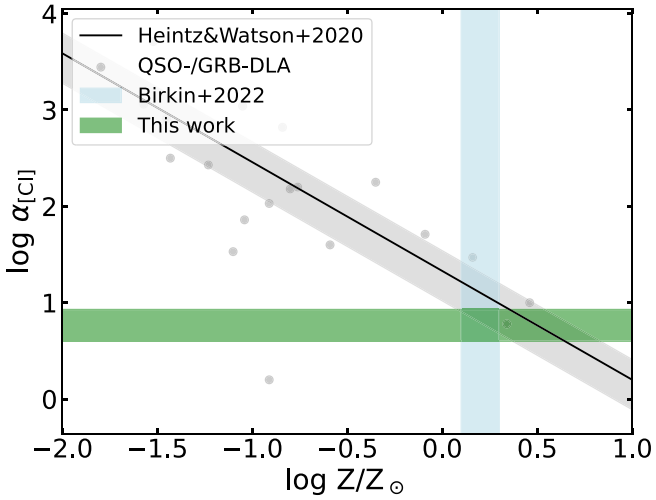

Figure 8. [C I] conversion factor $\alpha_{[C\,I]}$ as a function of metallicity. The dark green band marks the value derived using $X_{[C\,I]}$=(5.1 ± 1.8) × 10^{-5} for the sample of SMGs presented in this work. The light green band marks the SMG metallicities derived from [N II]/Hα by J. E. Birkin (2022). The black line represents the best-fit linear relation log $\alpha_{[C\,I]} = -1/13 \times \log Z/Z_\odot + 1.33$ from K. E. Heintz & D. Watson (2020). The solar/supersolar metallicities derived support the use of a higher (lower) $X_{[C\,I]}$ (α_{CO}) in SMGs, rather than a universal value for different galaxy populations.

5. Conclusions

We have presented ALMA Band 3 and 4 observations targeting [C I](1–0) in a sample of 12 $z \sim 2$–5 unlensed, massive, gas-rich galaxies with CO(1–0) observations from a new VLA survey of molecular gas in massive star-forming galaxies at high redshift (M. Frias Castillo et al. 2023). Combining these data with eight archival detections in the

CO(1–0) sample, we have compiled a total of 20 galaxies with observations of the ground-state transitions of both species. This data set allows us to directly compare CO(1–0) and [C I](1–0) as tracers of the cold molecular gas reservoirs in galaxies at high redshift. The main conclusions are as follows:

1. We detect [C I](1–0) line emission at $\geqslant 2\sigma$ in 10 out of 12 galaxies observed. The full sample has [C I](1–0) line luminosities in the range 1.2–3.1 $\times 10^{10}$ K km s^{-1} pc^2. The [C I](1–0)/CO(1–0) line luminosity ratio is consistent with the one found at lower redshifts for ULIRGs and main-sequence galaxies, and shows no deviation out to $z \sim 5$.
2. Combining the mid–$J_{\rm up}$ CO and [C I] line luminosities with infrared luminosities, we constrain the conditions of the ISM of our sample using PDR models. We find a median density $\log(n[{\rm cm}^{-3}]) = 4.7 \pm 0.2$, and a median UV radiation field $\log(G_{\rm UV}[G_0]) = 3.2 \pm 0.2$. There is a significant overlap in the parameter space occupied by our sources and local ULIRGs, $z \sim 1$ main-sequence galaxies, and published high-redshift SMGs.
3. We compare our measurements of $L'_{\rm CO(1-0)}$, $L'_{\rm [CI](1-0)}$, and 3mm dust continuum to provide a cross-calibration for their conversion factors, $\alpha_{\rm CO}$, $X_{\rm [C\,I]}$, and α_{850}, respectively. The conversion factors do not evolve with redshift or $L_{\rm IR}$. We find that the product $X_{\rm [C\,I]} \times \alpha_{\rm CO}$ is remarkably similar for local ULIRGs, main-sequence galaxies, and high-redshift SMGs, and this affects the derived $X_{\rm [C\,I]}$ values when different values of $\alpha_{\rm CO}$ are assumed for various galaxy populations. Taking $\alpha_{\rm CO} = 1$ for our sample of SMGs, we derive a median $X_{\rm [C\,I]} = (5.1 \pm 1.8) \times 10^{-5}$. This results in gas masses $M_{\rm H_2,[CI]}$ in the range 5–21 $\times 10^{10} M_\odot$. Likewise, these choices of $\alpha_{\rm CO}$ and $X_{\rm [CI]}$ result in values of $\alpha_{850} = (2.2 \pm 1.0) \times 10^{20}$ erg s^{-1} Hz^{-1} $M_\odot^{-1}$ and $(2.4 \pm 1.0) \times 10^{20}$ erg s^{-1} Hz^{-1} $M_\odot^{-1}$, respectively. These values differ from the canonically assumed $X_{\rm [C\,I]} = 3 \times 10^{-5}$ and $\alpha_{850} = 4.4 \times 10^{20}$ erg s^{-1} Hz^{-1} $M_\odot^{-1}$, but are supported by predictions for the solar/supersolar metallicities expected for our sources.
4. We model the effect of the warmer CMB at high redshift on the measured intensities of CO(1–0) and [C I](1–0). The absolute effect on both individual lines can be quite severe, but the relative effect between the lines is much smaller, such that the ratio between the lines decreases by up to ∼30% for the coldest gas kinetic temperatures expected. A comparison of the $L'_{\rm CO(1-0)}/L'_{\rm [CI](1-0)}$ ratio between local ULIRGs and our sources shows both populations have similar values, suggesting that the ratio is not obviously suppressed out to $z \sim 5$.

We caveat that current constraints on the conversion factors at high redshift are limited to typically very active sources. To improve the calibration of $X_{\rm [C\,I]}$, $\alpha_{\rm CO}$, and α_{850} at high redshift, as well as the constraints on the effects of the CMB, it is necessary to obtain samples of galaxies spanning a larger range of masses and metallicities. Additionally, well-sampled CO and [C I] SLEDs will facilitate a more accurate modeling of properties of their cold ISM. The galaxies presented in this work constitute the largest sample of unlensed galaxies with CO(1–0) and [C I(1–0)] observations, which will be crucial for understanding the physical conditions of cold ISM at high redshift.

Acknowledgments

This paper makes use of the following ALMA data: ADS/JAO.ALMA#2021.1.01342.S. ALMA is a partnership of ESO (representing its member states), NSF (USA), and NINS (Japan), together with NRC (Canada), Molonglo Observatory Synthesis Telescope (MOST) and ASIAA (Taiwan), and KASI (Republic of Korea), in cooperation with the Republic of Chile. The Joint ALMA Observatory is operated by ESO, AUI/NRAO, and NAOJ. This paper makes use of data from the IRAM/NOEMA program S19CV (PI: Chapman). M.R. is supported by the NWO Veni project "Under the lens" (VI. Veni.202.225). J.H. acknowledges support from the ERC Consolidator grant 101088676 (VOYAJ) and the VIDI research program with project No. 639.042.611, which is (partly) financed by the Netherlands Organisation for Scientific Research (NWO). J.B. has received funding from the European Research Council (ERC) under the European Union's Horizon 2020 research and innovation program MOPPEX 833460. Part of this work was supported by the German Deutsche Forschungsgemeinschaft, DFG project No. Ts 17/2–1. T.T. gratefully acknowledges the Collaborative Research Center 1601 (SFB 1601 subproject A6) funded by the Deutsche Forschungsgemeinschaft (DFG, German Research Foundation)—500700252. C.C.C. and C.-L.L. acknowledge support from the National Science and Technology Council of Taiwan (NSTC 111-2112M-001-045-MY3), as well as Academia Sinica through the Career Development Award (AS-CDA-112-M02). I.R.S. and A.M.S. acknowledge support from STFC (ST/T000244/1 and ST/X001075/1). E. F.J.-A. acknowledges support from UNAM-PAPIIT project IA102023, and from CONAHCyT Ciencia de Frontera project ID: CF-2023-I-506. H.D. acknowledges financial support from the Agencia Estatal de Investigación del Ministerio de Ciencia e Innovación (AEI-MCINN) under grant (La evolución de los cúmulos de galaxias desde el amanecer hasta el mediodìa cósmico) with reference (PID2019-105776GB-I00/DOI:10.13039/501100011033) and the Ministerio de Ciencia, Innovación y Universidades (MCIU/AEI) under grant (Construcción de cúmulos de galaxias en formación a través de la formación estelar oscurecida por el polvo) and the European Regional Development Fund (ERDF) with reference (PID2022-143243NB-I00/DOI:10.13039/501100011033). This work was supported by NAOJ ALMA Scientific Research grant Code 2021-19A (H.S.B.A). The National Radio Astronomy Observatory is a facility of the National Science Foundation operated under cooperative agreement by Associated Universities, Inc. The authors acknowledge assistance from Allegro, the European ALMA Regional Center node in the Netherlands.

Appendix
Cosmic Microwave Background Effect on Dust Emission

In Section 3.4, we evaluated the impact of elevated CMB temperature on the observed CO(1-0) and [CI](1-0) emission. For completeness, we perform the same test for dust continuum emission at an observed-frame frequency of 100 GHz. Figure 9 shows the resulting signal attenuation, and the impact on the CO(1-0)/$S_{850\mu{\rm m}}$ and [CI](1-0)/$S_{850\,\mu{\rm m}}$ ratios.

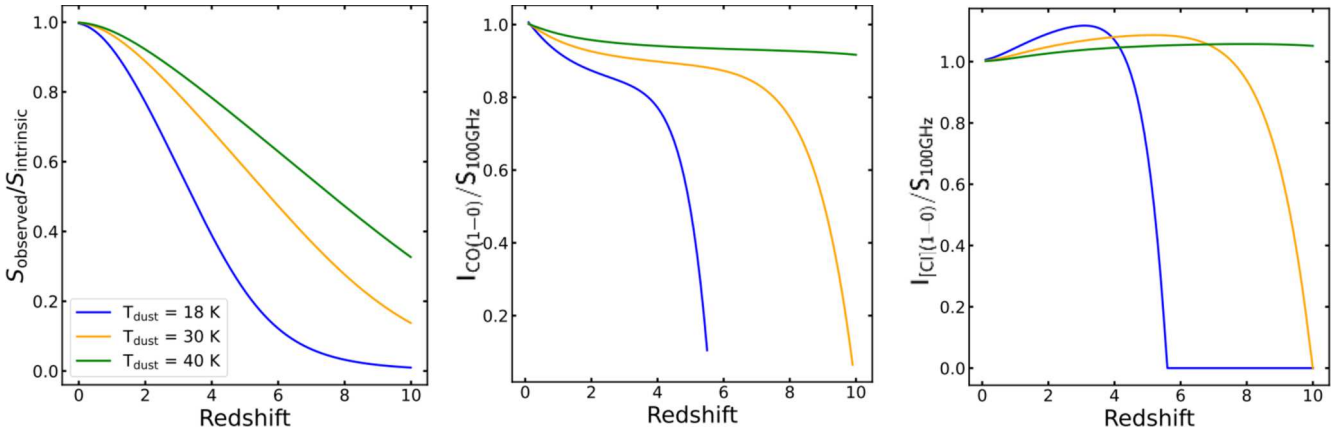

Figure 9. Effect of the warmer CMB on the recovered dust emission at 100 GHz as a function of redshift. We assume three different T_{dust} at $z = 0$, and plot the ratio between the intrinsic flux emitted by that galaxy at $z = 0$ and what can be recovered as the warmer CMB increases in temperature at higher redshift.

For $T_{dust} = 30$ K, the CO/dust and [C I]/dust flux ratios are approximately constant out to $z = 6$, as the effect of the CMB is of a similar order of magnitude for all tracers individually.

ORCID iDs

Marta Frias Castillo https://orcid.org/0000-0002-9278-7028
Matus Rybak https://orcid.org/0000-0002-1383-0746
Jacqueline A. Hodge https://orcid.org/0000-0001-6586-8845
Paul van der Werf https://orcid.org/0000-0001-5434-5942
Ian Smail https://orcid.org/0000-0003-3037-257X
Joshua Butterworth https://orcid.org/0000-0002-5353-1775
Theodoros Topkaras https://orcid.org/0000-0001-9143-1495
Chian-Chou Chen https://orcid.org/0000-0002-3805-0789
Axel Weiss https://orcid.org/0000-0003-4678-3939
Hiddo Algera https://orcid.org/0000-0002-4205-9567
Jack E. Birkin https://orcid.org/0000-0002-3272-7568
Elisabete da Cunha https://orcid.org/0000-0001-9759-4797
Jianhang Chen https://orcid.org/0000-0003-3921-3313
Helmut Dannerbauer https://orcid.org/0000-0001-7147-3575
E. F. Jiménez-Andrade https://orcid.org/0000-0002-2640-5917
Cheng-Lin Liao https://orcid.org/0000-0002-5247-6639
Eric J. Murphy https://orcid.org/0000-0001-7089-7325
A.M. Swinbank https://orcid.org/0000-0003-1192-5837
Fabian Walter https://orcid.org/0000-0003-4793-7880
Gabriela Calistro Rivera https://orcid.org/0000-0003-0085-6346
R. J. Ivison https://orcid.org/0000-0001-5118-1313
Claudia del P. Lagos https://orcid.org/0000-0003-3021-8564

References

Alaghband-Zadeh, S., Chapman, S. C., Swinbank, A. M., et al. 2013, MNRAS, 435, 1493
Amvrosiadis, A., Wardlow, J. L., Birkin, J. E., et al. 2023, MNRAS, 536, 3757
Andreani, P., Retana-Montenegro, E., Zhang, Z.-Y., et al. 2018, A&A, 615, A142
Aravena, M., Spilker, J. S., Bethermin, M., et al. 2016, MNRAS, 457, 4406
Battisti, A. J., da Cunha, E., Grasha, K., et al. 2019, ApJ, 882, 61
Berta, S., Stanley, F., Ismail, D., et al. 2023, A&A, 678, A28
Béthermin, M., Daddi, E., Magdis, G., et al. 2015, A&A, 573, A113
Birkin, J. E. 2022, PhD thesis, Durham Univ., UK
Birkin, J. E., Hutchison, T. A., Welch, B., et al. 2023, ApJ, 958, 64
Birkin, J. E., Weiss, A., Wardlow, J. L., et al. 2021, MNRAS, 501, 3926
Bisbas, T. G., Tan, J. C., & Tanaka, K. E. I. 2021, MNRAS, 502, 2701
Bolatto, A. D., Wolfire, M., & Leroy, A. K. 2013, ARA&A, 51, 207
Boogaard, L. A., van der Werf, P., Weiss, A., et al. 2020, ApJ, 902, 109
Bothwell, M. S., Aguirre, J. E., Aravena, M., et al. 2017, MNRAS, 466, 2825
Bothwell, M. S., Smail, I., Chapman, S. C., et al. 2013, MNRAS, 429, 3047
Bothwell, M. S., Wagg, J., Cicone, C., et al. 2014, MNRAS, 445, 2599
Bourne, N., Dunlop, J. S., Simpson, J. M., et al. 2019, MNRAS, 482, 3135
Cañameras, R., Yang, C., Nesvadba, N. P. H., et al. 2018, A&A, 620, A61
Calistro Rivera, G., Hodge, J. A., Smail, I., et al. 2018, ApJ, 863, 56
Carilli, C. L., & Walter, F. 2013, ARA&A, 51, 105
Chen, C.-C., Hodge, J. A., Smail, I., et al. 2017, ApJ, 846, 108
Chen, C.-C., Liao, C.-L., Smail, I., et al. 2022, ApJ, 929, 159
Cormier, D., Bigiel, F., Jiménez-Donaire, M. J., et al. 2018, MNRAS, 475, 3909
da Cunha, E., Groves, B., Walter, F., et al. 2013, ApJ, 766, 13
da Cunha, E., Hodge, J. A., Casey, C. M., et al. 2021, ApJ, 919, 30
da Cunha, E., Walter, F., Smail, I. R., et al. 2015, ApJ, 806, 110
Danielson, A. L. R., Swinbank, A. M., Smail, I., et al. 2011, MNRAS, 410, 1687
Dannerbauer, H., Harrington, K., Díaz-Sánchez, A., et al. 2019, AJ, 158, 34
De Breuck, C., Williams, R. J., Swinbank, M., et al. 2014, A&A, 565, A59
Decarli, R., Aravena, M., Boogaard, L., et al. 2020, ApJ, 902, 110
Dessauges-Zavadsky, M., Ginolfi, M., Pozzi, F., et al. 2020, A&A, 643, A5
Downes, D., & Solomon, P. M. 1998, ApJ, 507, 615
Dudzevičiūtė, U., Smail, I., Swinbank, A. M., et al. 2020, MNRAS, 494, 3828
Dunne, L., Maddox, S. J., Papadopoulos, P. P., Ivison, R. J., & Gomez, H. L. 2022, MNRAS, 517, 962
Eales, S., Gomez, H., Dunne, L., Dye, S., & Smith, M. W. L. 2024, MNRAS, 532, 2905
Frayer, D. T., Harris, A. I., Baker, A. J., et al. 2011, ApJL, 726, L22
Frias Castillo, M., Hodge, J., Rybak, M., et al. 2023, ApJ, 945, 128
Frias Castillo, M., Rybak, M., Hodge, J., et al. 2022, ApJ, 930, 35
Geach, J. E., Dunlop, J. S., Halpern, M., et al. 2017, MNRAS, 465, 1789
Greve, T. R., Bertoldi, F., Smail, I., et al. 2005, MNRAS, 359, 1165
Gururajan, G., Béthermin, M., Sulzenauer, N., et al. 2023, A&A, 676, A89
Habing, H. J. 1968, BAN, 19, 421
Hainline, L. J., Blain, A. W., Greve, T. R., et al. 2006, ApJ, 650, 614
Harrington, K. C., Weiss, A., Yun, M. S., et al. 2021, ApJ, 908, 95
Harrington, K. C., Yun, M. S., Magnelli, B., et al. 2018, MNRAS, 474, 3866
Harris, A. I., Baker, A. J., Frayer, D. T., et al. 2012, ApJ, 752, 152
Heintz, K. E., & Watson, D. 2020, ApJL, 889, L7
Hildebrand, R. H. 1983, QJRAS, 24, 267
Hill, R., Chapman, S. C., Scott, D., et al. 2018, MNRAS, 477, 2042
Hodge, J. A., Carilli, C. L., Walter, F., et al. 2012, ApJ, 760, 11
Hodge, J. A., & da Cunha, E. 2020, RSOS, 7, 200556
Hollenbach, D. J., & Tielens, A. G. G. M. 1999, RvMP, 71, 173
Hughes, D. H., Serjeant, S., Dunlop, J., et al. 1998, Natur, 394, 241
Huynh, M. T., Emonts, B. H. C., Kimball, A. E., et al. 2017, MNRAS, 467, 1222
Ikeda, M., Oka, T., Tatematsu, K., Sekimoto, Y., & Yamamoto, S. 2002, ApJS, 139, 467
Israel, F. P., Rosenberg, M. J. F., & van der Werf, P. 2015, A&A, 578, A95
Ivison, R. J., Papadopoulos, P. P., Smail, I., et al. 2011, MNRAS, 412, 1913
Jarugula, S., Vieira, J. D., Weiss, A., et al. 2021, ApJ, 921, 97
Jiao, Q., Zhao, Y., Lu, N., et al. 2019, ApJ, 880, 133
Jiao, Q., Zhao, Y., Zhu, M., et al. 2017, ApJL, 840, L18

Jin, S., Daddi, E., Magdis, G. E., et al. 2019, ApJ, 887, 144
Jin, S., Daddi, E., Magdis, G. E., et al. 2022, A&A, 665, A3
Kaasinen, M., Scoville, N., Walter, F., et al. 2019, ApJ, 880, 15
Kamenetzky, J., Rangwala, N., Glenn, J., Maloney, P. R., & Conley, A. 2016, ApJ, 829, 93
Kaufman, M. J., Wolfire, M. G., & Hollenbach, D. J. 2006, ApJ, 644, 283
Keene, J., Lis, D. C., Phillips, T. G., & Schilke, P. 1997, in IAU Symp. 178, Molecules in Astrophysics: Probes and Processes (Cambridge: Cambridge Univ. Press), 129
Kelly, B. C. 2007, ApJ, 665, 1489
Kennicutt, R. C., Jr. 1998, ApJ, 498, 541
Kennicutt, R. C., & Evans, N. J. 2012, ARA&A, 50, 531
Liao, C.-L., Chen, C.-C., Wang, W.-H., et al. 2024, ApJ, 961, 226
Liu, D., Schinnerer, E., Groves, B., et al. 2019, ApJ, 887, 235
Magdis, G. E., Daddi, E., Elbaz, D., et al. 2011, ApJL, 740, L15
Magnelli, B., Lutz, D., Santini, P., et al. 2012, A&A, 539, A155
McMullin, J. P., Waters, B., Schiebel, D., Young, W., & Golap, K. 2007, in ASP Conf. Ser. 376, Astronomical Data Analysis Software and Systems XVI, ed. R. A. Shaw, F. Hill, & D. J. Bell (San Francisco, CA: ASP), 127
Montoya Arroyave, I., Cicone, C., Makroleivaditi, E., et al. 2023, A&A, 673, A13
Nesvadba, N. P. H., Cañameras, R., Kneissl, R., et al. 2019, A&A, 624, A23
Ojha, R., Stark, A. A., Hsieh, H. H., et al. 2001, ApJ, 548, 253
Papadopoulos, P., Dunne, L., & Maddox, S. 2022, MNRAS, 510, 725
Papadopoulos, P. P., & Greve, T. R. 2004, ApJL, 615, L29
Papadopoulos, P. P., Thi, W. F., & Viti, S. 2004, MNRAS, 351, 147
Papadopoulos, P. P., van der Werf, P. P., Xilouris, E. M., et al. 2012, MNRAS, 426, 2601
Planck Collaboration, Ade, P. A. R., Aghanim, N., et al. 2016, A&A, 594, A13
Popping, G., & Péroux, C. 2022, MNRAS, 513, 1531
Popping, G., Decarli, R., Man, A. W. S., et al. 2017, A&A, 602, A11
Popping, G., Shivaei, I., Sanders, R. L., et al. 2023, A&A, 670, A138
Pound, M. W., & Wolfire, M. G. 2008, in ASP Conf. Ser. 394, Astronomical Data Analysis Software and Systems XVII, ed. R. W. Argyle, P. S. Bunclark, & J. R. Lewis (San Francisco, CA: ASP), 654
Remy, Q., Grenier, I. A., Marshall, D. J., & Casandjian, J. M. 2017, A&A, 601, A78
Riechers, D. A., Boogaard, L. A., Decarli, R., et al. 2020a, ApJL, 896, L21
Riechers, D. A., Hodge, J. A., Pavesi, R., et al. 2020b, ApJ, 895, 81
Rigopoulou, D., Pereira-Santaella, M., Magdis, G. E., et al. 2018, MNRAS, 473, 20
Rybak, M., Hodge, J. A., Vegetti, S., et al. 2020, MNRAS, 494, 5542
Rybak, M., van Marrewijk, J., Hodge, J. A., et al. 2023, A&A, 679, A119
Saintonge, A., Catinella, B., Tacconi, L. J., et al. 2017, ApJS, 233, 22
Saintonge, A., Lutz, D., Genzel, R., et al. 2013, ApJ, 778, 2
Sandstrom, K. M., Leroy, A. K., Walter, F., et al. 2013, ApJ, 777, 5
Schmidt, M. 1959, ApJ, 129, 243
Schöier, F. L., van der Tak, F. F. S., van Dishoeck, E. F., & Black, J. H. 2005, A&A, 432, 369
Scoville, N., Lee, N., Vanden Bout, P., et al. 2017, ApJ, 837, 150
Scoville, N., Sheth, K., Aussel, H., et al. 2016, ApJ, 820, 83
Sharon, C. E., Riechers, D. A., Hodge, J., et al. 2016, ApJ, 827, 18
Simpson, J. M., Smail, I., Dudzevičiūtė, U., et al. 2020, MNRAS, 495 3409
Simpson, J. M., Smail, I., Swinbank, A. M., et al. 2019, ApJ, 880, 43
Smail, I., Ivison, R. J., & Blain, A. W. 1997, ApJL, 490, L5
Solomon, P. M., & Vanden Bout, P. A. 2005, ARA&A, 43, 677
Stach, S. M., Dudzevičiūtė, U., Smail, I., et al. 2019, MNRAS, 487, 4648
Stach, S. M., Smail, I., Swinbank, A. M., et al. 2018, ApJ, 860, 161
Swinbank, A. M., Simpson, J. M., Smail, I., et al. 2014, MNRAS, 438, 1267
Tacconi, L. J., Genzel, R., Neri, R., et al. 2010, Natur, 463, 781
Tacconi, L. J., Genzel, R., Smail, I., et al. 2008, ApJ, 680, 246
Tacconi, L. J., Genzel, R., & Sternberg, A. 2020, ARA&A, 58, 157
Tacconi, L. J., Neri, R., Genzel, R., et al. 2013, ApJ, 768, 74
Thomson, A. P., Ivison, R. J., Smail, I., et al. 2012, MNRAS, 425, 2203
Tielens, A. G. G. M., & Hollenbach, D. 1985, ApJ, 291, 722
Tomassetti, M., Porciani, C., Romano-Diaz, E., Ludlow, A. D., & Papadopoulos, P. P. 2014, MNRAS, 445, L124
Valentino, F., Daddi, E., Puglisi, A., et al. 2020, A&A, 641, A155
Valentino, F., Magdis, G. E., Daddi, E., et al. 2018, ApJ, 869, 27
van der Tak, F. F. S., Black, J. H., Schöier, F. L., Jansen, D. J., & van Dishoeck, E. F. 2007, A&A, 468, 627
Walter, F., Carilli, C., Neeleman, M., et al. 2020, ApJ, 902, 111
Walter, F., Weiß, A., Downes, D., Decarli, R., & Henkel, C. 2011, ApJ, 730, 18
Wang, T.-M., Magnelli, B., Schinnerer, E., et al. 2022, A&A, 660, A142
Weiß, A., Downes, D., Henkel, C., & Walter, F. 2005, A&A, 429, L25
Weiß, A., Henkel, C., Downes, D., & Walter, F. 2003, A&A, 409, L41
Xue, R., Fu, H., Isbell, J., et al. 2018, ApJL, 864, L11
Yang, C., Omont, A., Beelen, A., et al. 2017, A&A, 608, A144
Zhang, Z.-Y., Papadopoulos, P. P., Ivison, R. J., et al. 2016, RSOS, 3, 160025